Absolute calibration of the ratio of Xe/O two-photon absorption cross-sections for O-TALIF applications

Z Shu, N Popov, S Starikovskaia

Absolute calibration of the ratio of Xe/O two–photon absorption cross-sections for O-TALIF applications

Z Shu[1], N A Popov[2], S M Starikovskaia[1]

[1] Laboratory of Plasma Physics (CNRS, Ecole Polytechnique, Univ. Paris-Sud, Observatoire de Paris, Sorbonne Université, l'Institut Polytechnique de Paris), Ecole Polytechnique, route de Saclay, 91128 Palaiseau, France

[2] Skobeltsyn Institute of Nuclear Physics, Moscow State University, Moscow, 119991, Leninsky gory, Russia

E-mail: svetlana.starikovskaia@lpp.polytechnique.fr
zhan.shu@lpp.polytechnique.fr

Abstract. The paper presents a calibration of the ratio of two-photon absorption cross sections, $\sigma^{(2)}_{Xe}/\sigma^{(2)}_{O}$, necessary for the absolute O-atom density measurements by two-photon absorption laser-induced fluorescence (TALIF) technique. To calibrate the ratio of the cross-sections, a special discharge with 100% dissociation of molecular oxygen, and so with a known "reference" density of O-atom $[O]_{ref}$=2·$[O_2]$ was suggested. This is a nanosecond capillary discharge in N_2: O_2 mixtures with a few percent of oxygen at a reduced electric field of a few hundred of Td and specific deposited energy of about 1 eV/molecule. Voltage at the electrodes, electrical current in the plasma, longitudinal electric field and energy delivered to the gas were measured with 0.2 ns synchronisation. Additionally, radial distribution of emission of excited nitrogen molecules and gas temperature in the discharge and afterglow were obtained experimentally. Detailed 1D kinetic modeling was suggested to confirm complete O_2 dissociation and to analyse the main reactions. By comparing the data measured by TALIF technique with the "reference" density of oxygen atoms $[O]_{ref}$, the ratio of the two-photon absorption cross-sections $\sigma^{(2)}_{Xe}/\sigma^{(2)}_{O}$ was determined.

Keywords: TALIF, Xe/O cross-sections, absolute calibration, plasma, nanosecond discharge, kinetics, spectroscopy

1. Introduction

Most low-temperature plasma physics problems require quantitative plasma characterisation, whereas the exchange and dissemination of results require standardisation of the measurement process [1]. Standardisation means having a procedure that recommends the best practices and produces results that will be used by the community in the most efficient, reliable, reproducible, and least ambiguous manner. This statement fully applies to the measurement of atomic density in plasma and afterglow of gas discharges.

1.1. Historical retrospective

Atomic species are readily produced in reactive media, such as discharge or combustion environments. These atoms are not homogeneous in space, exhibit, being radicals, considerable chemical reactivity in their ground state, and their lifetime is often too short to be able to measure their density by standard chemical methods. Two-photon absorption laser-induced fluorescence (TALIF), offers a well-suited technique for detecting main atomic species, such as O, H, and N, with sub-millimeter spatial resolution and high temporal resolution, using nanosecond [2], picosecond and femtosecond lasers [3].

O-TALIF was initially developed in the 1980s as a gas discharge diagnostics tool, suitable for relatively low gas densities, typically less than 1 mbar [4]. The difficulties related to the broad gap of energy and necessity to use VUV light for excitation of fluorescence of atoms from the ground state, were overcome by using simultaneous absorption of two photons in the UV region at $\lambda \approx 225.7$ nm. Around the same time, theoretical calculations [5] and measurements [6] of two-photon absorption cross-sections in atomic oxygen were proposed. However, obtaining the absolute atom densities was intricate, akin to an art form, and involved precise calibration of all the components of the diagnostic facility.

Review papers from that period discussing TALIF experiments in plasmas [7] merely mentioned the potential of two-photon diagnostics for H, N, S, and Cl atoms. A similar situation persisted in combustion studies, even at the beginning of the 2000s, where TALIF was seldom employed [8]. The challenges in using TALIF in combustion experiments included possible excitation of other species or additional production of the measured ones in chemically active mixtures, quenching in a chemically changing environment, and absolute calibration.

During this early stage of LIF/TALIF diagnostics development, calibration, especially for the single-photon LIF technique, was frequently achieved through direct comparison with other well-established techniques, such as laser absorption and/or photolysis measurements [9]. In addition, in combustion experiments, calibration was sometimes performed by comparing results with numerical modeling under well-defined, thermodynamically equilibrium, typically laminar flame conditions [10].

1.2. TALIF calibration on noble gases

The situation with TALIF changed in a revolutionary way about 20 years ago following the publication of a series of papers [11,12]. A novel calibration method for determining absolute atomic densities was proposed, based on a comparative measurement with a noble gas that exhibits a two-photon resonance closely matching the transition under investigation. The two-photon resonances of H-atoms ($\lambda = 2 \times 205.08$ nm), N-atoms ($\lambda = 2 \times 206.65$ nm) and O-atom ($\lambda = 2 \times 225.58$ nm) were investigated together with two selected transitions in their "homologues", namely Kr ($\lambda = 2 \times 204.13$ nm) for H and N atoms and Xe ($\lambda = 2 \times 225.44$ nm) for O-atom. The natural lifetimes of the excited states, quenching coefficients for the most important collision partners, and the relevant ratios of the two-photon absorption cross sections were measured, providing a "kit" for experimentally simple and accessible calibration of densities of atoms. The ratios of the cross-sections were based on comparative measurements by TALIF and titration [12].

Will note that the excitation scheme suggested in [11, 12], considered xenon two-photon resonance $5p^6\ ^1S_0 \rightarrow 7p[3/2]_2$, 225.44 nm and atomic oxygen $2p^4\ ^3P_2 \rightarrow 3p\ ^3P_J$, 225.58 nm with a fluorescence of 7p $\rightarrow$ 6s transition for Xe at 462.43 nm, and fluorescence of 3p $\rightarrow$ 3s transition for O at 844.64 nm respectively. The authors claimed that they estimated the ratio of two-photon absorption cross-sections, $\sigma^{(2)}_{Xe}/\sigma^{(2)}_{O}$, "to be correct to 50% in view of the various input parameters and the reproducibility of the laser beam profile".

In later paper [13], the same authors suggested an alternative scheme for Xe TALIF. They reported xenon two-photon resonance $5p^6\ ^1S_0 \rightarrow 6p'[3/2]_2$, 224.31 nm with a fluorescence of $6p' \rightarrow 6s'$ transition for Xe at 834.91 nm. The excitation of atomic oxygen was similar to [12], $2p^4\ ^3P_2 \rightarrow 3p\ ^3P_J$, 225.65 nm with a fluorescence of 3p $\rightarrow$ 3s transition for O at 844.87 nm. This new scheme allowed using the same interference filter and a red-sensitive photomultiplier, with the fluorescence wavelengths for Xe and O being closer. Similar to [12], the authors performed calibration through titration and provided a "kit" for O-TALIF measurements, including radiative lifetimes, room temperature quenching coefficients, and the ratio of the cross-sections $\sigma^{(2)}_{Xe}/\sigma^{(2)}_{O}$ for this new excitation scheme [13]:

$$\sigma^{(2)}_{Xe} / \sum_{J'} \sigma^{(2)}_{O(J \rightarrow J')} = 1.9, \tag{1}$$

with the uncertainty being equal to $\pm 20\%$.

As a result of this easy-to-use calibration approach, TALIF measurements in gas discharge physics became more popular than single-photon LIF measurements of radical densities over the last two decades, where simple and robust calibration remained a challenge. TALIF with Xe-calibration has become a routine method for oxygen density

measurements [14–19]. In recent years, the same principle of O-TALIF measurements has been extended to picosecond [20] and femtosecond [21] TALIF. For a more detailed analysis of the technique of TALIF diagnostics, including the latest developments, one can refer to the recent review [2].

1.3. On recent measurements of cross-sections for Xe

Review [2] highlights that two-photon absorption cross-sections are scarce in the literature. Only one group of authors has measured the ratio of two-photon absorption cross-sections [11–13]. Recently, more and more papers are being published where authors compare different techniques under similar experimental conditions.

Paper [22] provides a comparison of numerical simulation with the absolute densities of vibrational level obtained by high sensitivity absorption spectroscopy measurements of the Schumann–Runge bands for O_2(X, v = 4–18), O(^{3}P) atom by TALIF calibrated against Xe, and laser photodetachment measurements of the atomic oxygen negative ions. The authors remark that using the value of the ratio determined by [13] may overestimate the O atom density by up to a factor of two.

Paper [23] provides a direct comparison of absolute O-atom densities measured by picosecond TALIF [23] and by vacuum ultra-violet Fourier transform absorption spectroscopy (VUV-FTAS) [24]. Both experiments were performed in He COST-μAPPJ plasma jet with admixtures of H_2O at atmospheric pressure. Maximum O densities measured with ps-TALIF are about 70% of the O densities measured with VUV-FTAS. In spite of the fact that the experiments were performed under markedly different conditions (in the centre of the gap and at the nozzle exit, at different surface-to-volume ratios in the discharge zone), the authors [23] mention "two very different diagnostic techniques used and the uncertainties associated with them" as one of the possible reasons for the discrepancy.

Being inspired by the idea of direct re-calibration, the authors of [25, 26] decided to reevaluate the two-photon absorption cross-sections of Xe with the help of recording the fluorescence signal that follows the resonant absorption of two UV photons. The cross-section was found equal to $1.36^{+0.46}_{-0.34}$ and $1.88^{+0.75}_{-0.54} \times 10^{-43}$ m^4 for the $6p'[3/2]_2$, 224.3 nm and $6p'[1/2]_0$, 249.6 nm levels, respectively. For the $6p'[3/2]_2$, 224.3 nm level the measured cross-section appears more than a factor of 2 smaller than what had been deduced from the measured $\sigma^{(2)}_{Xe}/\sigma^{(2)}_{O}$ cross-section ratio [13] (see expression (1)) and the measured two-photon cross-section of oxygen at 225.6 nm [6], $\sigma^{(2)}(6p'[3/2]_2) = 1.9(2) \times 1.87(60) \times 10^{-43} = 3.6^{+1.7}_{-1.4} \times 10^{-43}$ m^4.

The ratio of the cross-sections, based on the measurements [25, 26] and providing almost 2 times smaller atomic oxygen density, was recently used [27] to compare O-

TALIF with THz absorption spectroscopy on the same capacitively coupled radio frequency oxygen discharge. Similar behavior of the atomic oxygen density was observed for both techniques when varying the applied power (20–100 W) and the gas pressure (0.7–1.3 mbar). Absolute values of O-atom density were systematically about 25% smaller compared to the THz absorption spectroscopy results.

1.4. Disadvantages of classical calibration techniques. New approach based on 100% O_2 dissociation at moderate gas pressures

The data variation discussed above requires an answer to the question of the accuracy of the TALIF calibration. One of the most controversial issues in noble gas calibration is the need to rely on a different technique to find out what the actual concentration of O atoms in the discharge is under the experimental conditions under which the calibration is performed.

This paper proposes a novel approach to address the calibration problem in TALIF data by using a discharge with the "reference" density of O-atom, $[O]_{ref}$. High-voltage pulsed nanosecond capillary discharges [28–30] operating at moderate pressures offer this unique opportunity. In these discharges, a N_2: O_2 mixture with a few percent of oxygen at a reduced electric field of a few hundreds of Townsend (Td) and specific deposited energy of about 1 eV/molecule achieves complete dissociation of molecular oxygen. Consequently, the O-atom density in the afterglow of the discharge is precisely known in advance, $[O]_{ref} = 2{\cdot}[O_2]_0$, where $[O_2]_0$ is the initial density of oxygen molecules. Numerical modeling presented in this paper proves 100% dissociation of O_2 under given experimental conditions and analyses the main pathways of production of atomic oxygen. By comparing the data measured by TALIF technique with the "reference" density of oxygen atoms $[O]_{ref}$, it becomes possible to determine the ratio of the two-photon absorption cross-sections $\sigma^{(2)}_{Xe}/\sigma^{(2)}_{O}$.

The paper is divided into the following sections. Section 2 describes the experimental setup of the nanosecond capillary discharge, the diagnostic techniques for measurements of parameters of the plasma and O-TALIF technique and approaches. Section 3 reports on experimental results of plasma parameters and density of oxygen atoms. Section 4 describes the numerical approach. Section 5 presents the results of calculation to verify the statement of complete dissociation of oxygen molecules and summarises the obtained information about the ratio of cross-sections. Finally, the accuracy of the experimental determination of the ratio of the cross-sections is discussed in the Appendix.

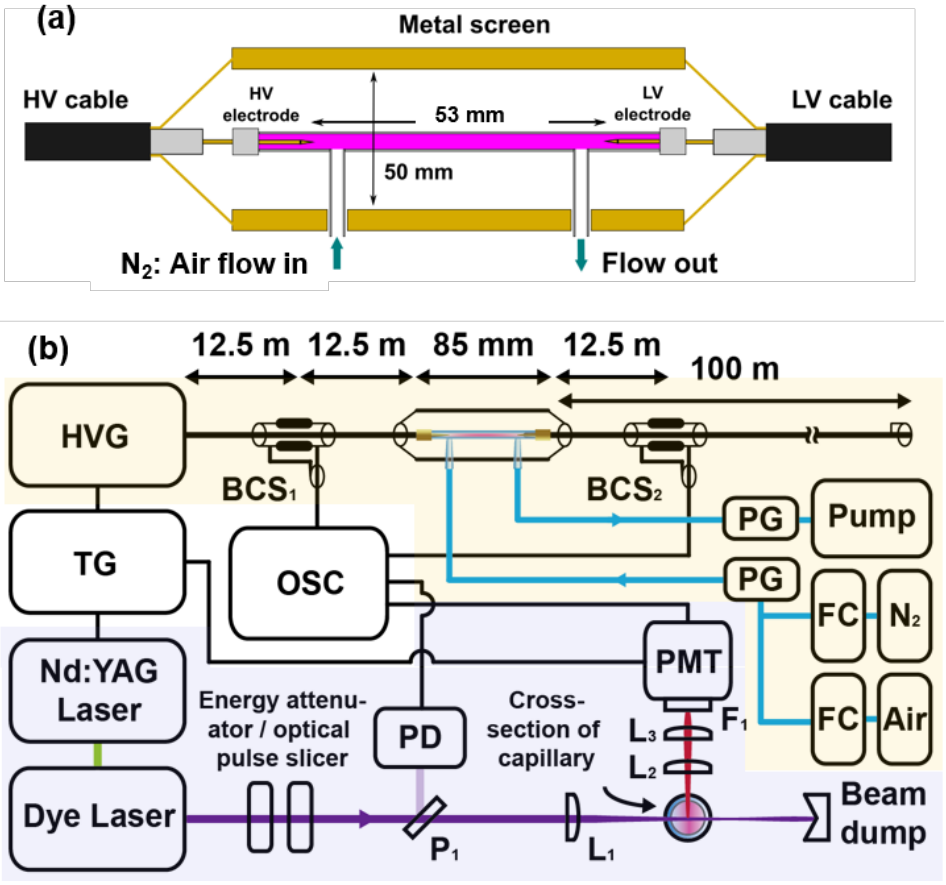

Figure 1. Schematic of the (a) discharge cell (b) experimental setup, including the discharge component (in yellow shadow) and the diagnostic component (in violet shadow). FC is mass flow controller, PG is pressure gauges, BCS is back current shunt, HVG is high voltage generator, TG is triggering generator, OSC is oscilloscope, PD is photodiode, PMT is photomultiplier tube.

2. Experimental setup and methods

2.1. Discharge setup and diagnostics

The schematic of the discharge cell is depicted in figure 1(a). The discharge was initiated in a quartz capillary tube with internal and external diameters of 2 mm and 4 mm, respectively. Two brass pin electrodes were inserted into both ends of the capillary, maintaining an inter-electrode distance of 53 mm. High voltage pulses of positive polarity, amplitude of 9.4 kV, rise time of 4 ns, full width at half maximum (FWHM) of 30 ns and repetitive frequency of 10 Hz, were produced by an FPG 12-1NM high-voltage generator (HVG) manufactured by FID GmbH. To deliver the pulses, an RG213 coaxial cable of 50 Ω impedance, 25 m in length, was connected to the high-voltage (HV) electrode. Another 100 m coaxial cable with a short-circuited end was connected to the low-voltage (LV) electrode. A 48 mm × 60 mm rectangular metal screen was connected to the grounded shielding of both the HV and LV cables, surrounding the

capillary tube. All electrical signals were recorded by a LeCroy WaveRunner 64Xi-A 600 MHz oscilloscope.

The incidence pulse generated by the HVG was partially reflected from the discharge cell due to a mismatch in wave resistance between the cable and plasma. Consequently, it propagated back through the cable and experienced a second reflection from the HVG. The reflections were blocked after 550 ns by the internal electrical circuit of the HVG. The propagation velocity of the electromagnetic signal along the polyethylene-insulated cable is $v = c/\sqrt{\varepsilon\mu} = 20\ \mathrm{cm \cdot ns^{-1}}$. As a result, a burst of three main pulses, separated by 245 ns, was applied to the discharge tube. Subsequently, the pulse sequence was repeated at 990 ns, resulting from the reflection of pulses transmitted through the LV delay cable. These pulses served solely as probe signals since their energy deposited into the plasma was negligible in comparison to the energy deposited by the main pulses.

Custom-made calibrated back current shunts (BCS) were used to measure the waveforms of the high-voltage pulses passing through the cables, as depicted in figure 1(b). $\mathrm{BCS_1}$ was employed to measure both the incident pulses (U_{inc}) from the HVG and the reflected pulses (U_{refl}) from the plasma, $\mathrm{BCS_2}$ was utilized to measure the pulses transmitted through the plasma (U_{tr}). The electrical current and voltage between the central wire and the shield of the cable are related by the equation $I = U/Z$, where the wave resistance Z equals 50 Ω. The longitudinal electric field E derived from the BCSs is expressed as:

$$E_{BCS}(t) = \frac{U_{refl}^{vac}(t) + U_{refl}(t) - U_{tr}(t)}{d}, \tag{2}$$

where U_{refl}^{vac} is the voltage pulse reflected from the discharge cell when no discharge occurs (e.g., at pressures below 10^{-2} mbar in the capillary), $d = 53$ mm is the inter-electrode distance. Another method to measure the longitudinal E-field is by the capacitive probe (CP) [31]. Custom-made calibrated CP was placed in a slit on top of the metal screen. By moving the CP along the discharge tube at 1 mm intervals, the electric potential as a function of distance x to the high-voltage electrode was measured. From the gradient of these electric potentials, the electric field is calculated as:

$$E_{CP}(t) = -\frac{\partial U_{cp}(x,t)}{\partial x}. \tag{3}$$

Then the energy W deposited in the plasma can be obtained by:

$$W = \int_0^{t_{pulse}} E_{CP}(t) \cdot d \cdot I_{tr}(t) dt, \tag{4}$$

where t_{pulse} represents the duration of the pulse and I_{tr} is the transmitted current measured by $\mathrm{BCS_2}$.

Pure nitrogen and air (80% N_2 + 20% O_2) from Air Liquide, with admixtures < 5.5 ppm, were used for the experiments. Two mass flow controllers, Brooks 5850TR and SLA5800, were employed to regulate the flow rates of N_2 and air, respectively. In varying oxygen ratios of 10%, 5% and 2%, the gas mixture was directed through the capillary via two side tubes positioned 4 mm apart from the electrodes. The total flow rate was maintained at 50 sccm, ensuring the gas renewal for each sequence of high-voltage pulses at 10 Hz. The static pressure in the middle of the capillary was kept at 27 mbar. The pressure was measured by taking the average readings of a pair of CMR362 capacitive pressure sensors (Pfeiffer Vacuum SAS), which were located symmetrically at equal distances before and after the discharge cell.

2.2. TALIF measurements

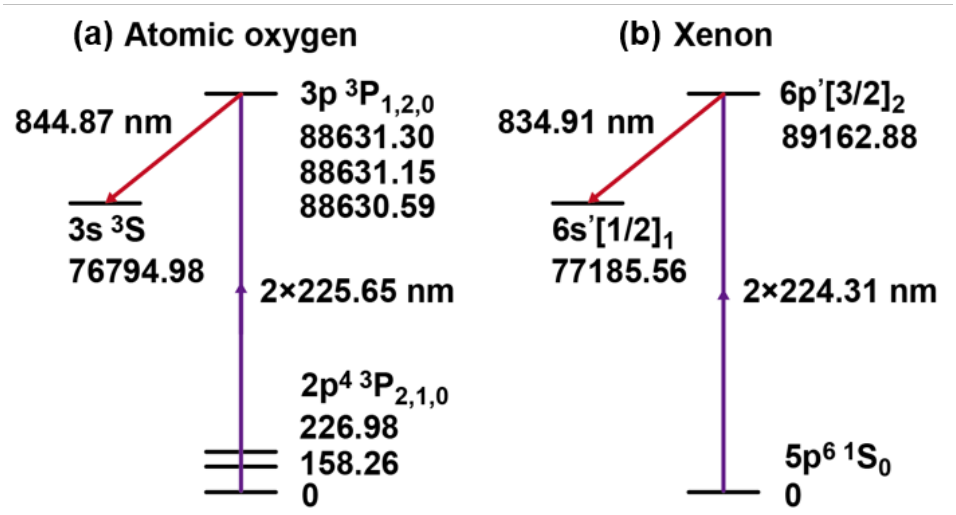

Figure 2. Two-photon excitation and fluorescence schemes for atomic oxygen and xenon (according to [13]). The level energies are given in cm^{-1}.

Figure 2(a) shows the O-TALIF scheme: the ground-state $O(2p^4\ ^3P_2)$ is excited to the $O(3p\ ^3P_{1,2,0})$ state by two 225.65 nm photons and subsequently fluoresces to the level of $O(3s\ ^3S)$, emitting light at 844.87 nm. To obtain quantitative atomic oxygen number densities, O-TALIF signal calibration is performed against $Xe(5p^6\ ^1S_0)$, which has a spectrally close two-photon resonance at 224.31 nm as shown in figure 2(b). The excited state $Xe(6p'[3/2]_2)$ then relaxes to the $Xe(6s'[1/2]_1)$ state, accompanied by the fluorescence at 834.91 nm. The temporally and spectrally integrated fluorescence signals S of these two species are written respectively:

$$S_O = \Gamma_O \cdot n_O \cdot \sigma_O^{(2)} \cdot \left(\frac{I_L^O}{h\nu_O}\right)^2 \cdot a_O \cdot F_O \cdot \eta_O \cdot f_{J=2}, \tag{5}$$

$$S_{Xe} = \Gamma_{Xe} \cdot n_{Xe} \cdot \sigma_{Xe}^{(2)} \cdot \left(\frac{I_L^{Xe}}{h\nu_{Xe}}\right)^2 \cdot a_{Xe} \cdot F_{Xe} \cdot \eta_{Xe}, \tag{6}$$

where Γ represents the two-photon statistical factor at a relevant laser wavelength, which is assumed to be invariant for atomic O and Xe since their resonances lie within close spectral proximity, n is the number density, $\sigma^{(2)}$ is the two-photon absorption cross-section, I_L is the laser intensity, h is the Planck constant, ν is the laser frequency. F stands for transmission of the optical filter, while η is the detector's quantum efficiency at the fluorescence wavelength. In addition, a is the effective branching ratio of the observed spontaneous transition $i \rightarrow j$:

$$a = \frac{A_{ij}}{A_i + Q_i}, \tag{7}$$

where $A_i = \sum_{j<i} A_{ij} = \tau_0^{-1}$ is the total spontaneous emission rate of the upper level, which is equal to the inverse of its natural radiative lifetime τ_0. $Q_i = \sum_q k_q^i n_q$ is the effective quenching rate, which is expressed by the collision partner densities n_q and the corresponding quenching coefficients k_q^i. The effective decay rate $A_i + Q_i$ can be determined by fitting the time-resolved fluorescence signal from experiments. $A_{ij} = A_i \cdot \frac{A_{ij}}{A_i}$ is calculated from the pure optical branching ratio where $Q_i = 0$. For atomic oxygen transition $3p\ ^3P_J \rightarrow 3s\ ^3S$, the ratio is equal to 1 [13], whereas for the used xenon transition $6p'[3/2]_2 \rightarrow 6s'[1/2]_1$ this value is 0.733 [32]. Therefore, the effective branching ratio can be further expressed as:

$$a_O = \frac{A_O}{A_O + Q_O}, \tag{8}$$

$$a_{Xe} = \frac{0.733 \cdot A_{Xe}}{A_{Xe} + Q_{Xe}}. \tag{9}$$

The fine structure of ground-state atomic oxygen needs to be considered due to the triplet states. Assuming the states are populated according to a Boltzmann distribution with the gas temperature T_g, the population fraction of the selected sub-levels $f_{J=2}$ is expressed as:

$$f_{J=2}(T_g) = \frac{(2J+1)\mathrm{e}^{-\frac{E_J}{k_B T_g}}}{\sum_{j=2,1,0}(2j+1)\mathrm{e}^{-\frac{E_j}{k_B T_g}}}, \tag{10}$$

with the state energy $E_2 = 0\ \mathrm{cm}^{-1}$, $E_1 = 158.27\ \mathrm{cm}^{-1}$, $E_0 = 226.98\ \mathrm{cm}^{-1}$ [13] and k_B is the Boltzmann constant. Finally, the number density of ground-state O-atom is given by comparing equations (5) and (6):

$$n_O = n_{Xe} \cdot \frac{\sigma_{Xe}^{(2)}}{\sigma_O^{(2)}} \cdot \frac{\nu_O^2}{\nu_{Xe}^2} \cdot \frac{0.733 \cdot A_{Xe}}{A_O} \cdot \frac{A_O + Q_O}{A_{Xe} + Q_{Xe}} \cdot \frac{F_{Xe}}{F_O} \cdot \frac{\eta_{Xe}}{\eta_O} \cdot \frac{I_{Xe}^2}{I_O^2} \cdot \frac{S_O}{S_{Xe}} \cdot \frac{1}{f_{J=2}}. \tag{11}$$

As illustrated in figure 1(b), the laser system consists of a frequency-doubled Quanta Ray Nd:YAG laser, which pumps a Sirah Lasertechnik Cobra Stretch dual-grating dye laser to generate the fundamental beam. This light is then frequency-tripled by two

successive alpha-BBO nonlinear crystals, to yield 3 mJ tunable UV pulses with a pulse duration of 6.5 ns and a repetition rate of 10 Hz. The UV beam, propagating along the capillary diameter, was focused by a 1-inch diameter, 50 cm focal length plano-convex lens (Thorlabs LA4184-ML). The focal point was set approximately at 1 cm after the capillary to avoid damaging the tube. The diameter of the laser beam at the entrance to the capillary was equal to 1 mm. A variable waveplate (Model 5540 Berek polarization compensator) and an alpha-BBO glan-laser polarizer (Thorlabs GLB10), namely energy attenuator, collectively modulated the laser intensity from 50 μJ to 350 μJ. A photodiode (Thorlabs DET10A) with rise time of 1 ns was used to monitor the laser intensity. The 2D spatial profile of the laser beam was checked by the camera beam profiler (Thorlabs BC106N-UV/M). It was proved that, for the two wavelengths employed for O-TALIF (225.65 nm) and Xe-TALIF (224.31 nm), the 2D distribution of light is similar.

Fluorescence was detected using Hamamatsu Photosensor Module H11526, an infrared-sensitive photomultiplier (PMT) with a gate function. The PMT was positioned atop the beam propagation axis and the capillary in an orthogonal configuration. Two 1-inch diameter plano-convex lenses, with focal lengths of 75 mm (Thorlabs LA4725) and 100 mm (Thorlabs LA4380) respectively, were employed to collimate and refocus the fluorescence light into the PMT. A bandpass filter centered at 850 nm (Thorlabs FBH850-40) was positioned in front of the PMT, blocking the emission from the plasma and scattered light from the UV probe laser. The time evolution of the O-atom density was measured by regulating the delay between the probe laser pulse and the discharge. To achieve this synchronization, a BNC 575 triggering generator (TG) was employed, which triggered the flash lamp and Q-switch of the Nd:YAG laser, the HVG and the gated PMT.

3. Experimental results

3.1. Plasma parameters measurements

3.1.1. Electric field, current and deposited energy in the discharge. According to the technique of BCS and CP mentioned above, the measured longitudinal reduced electric field E/N for three main discharge pulses in 27 mbar of N_2 + 10% O_2 mixture is plotted in figure 3. The red dashed line shows the back current shunt data scaled for synchronization in time of the CP and the BCS measurements. It was based on the fact that the waveforms of the Laplacian field measured by CP and BCS are similar and can be superimposed at a few first nanoseconds before the start of the discharge [28]. The accuracy of synchronization is equal to 0.2 ns. The shape of the first pulse is a classical fast ionization wave (FIW) field [33]. A sharp peak of E/N, 600 Td, is the FIW front, responsible for the initial ionization. In this period, the electric field is directed mainly radially from the axis of the discharge to the grounded screen, and the CP provides a

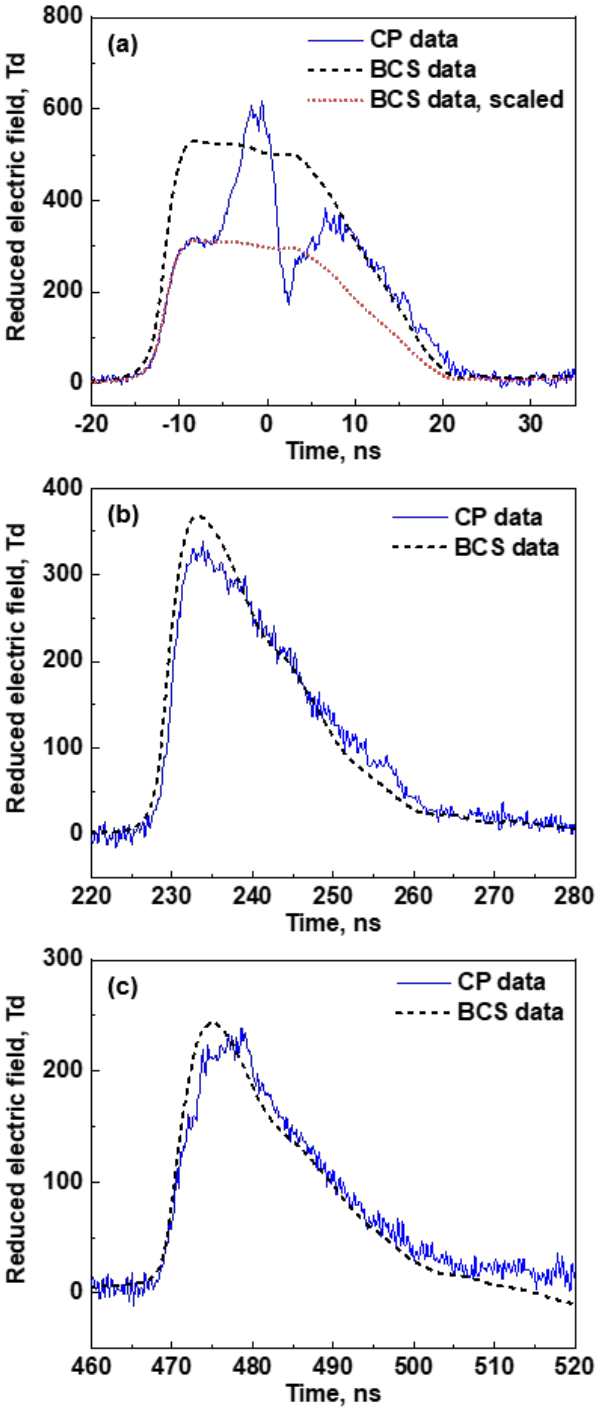

Figure 3. The longitudinal electric field measured by the capacitive probe (CP) technique and by the back current shunt (BCS) technique in 27 mbar of N_2 + 10% O_2 mixture for (a) the first third discharge pulse (dotted red line is the scaled BCS data used for synchronization of CP data with the BCS measurements), (b) the second third discharge pulse and (c) the third discharge pulse.

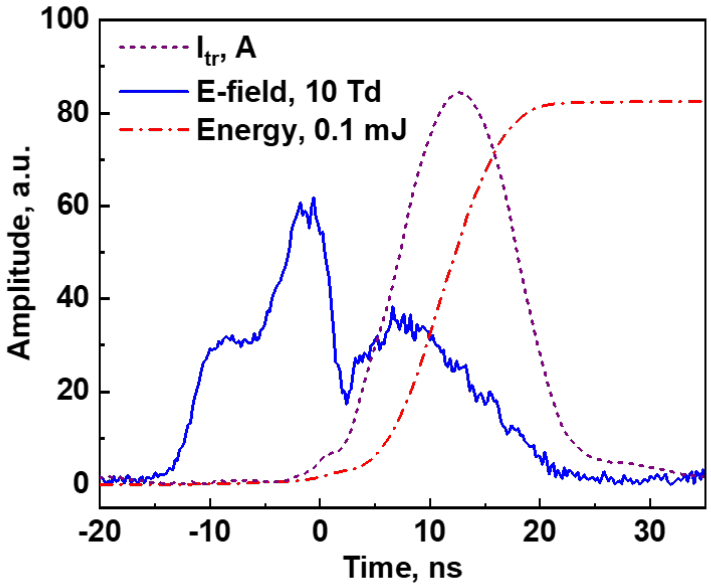

Figure 4. Synchronized profiles of the reduced electric field, transmitted current and deposited energy for the first pulse of N_2 + 10% O_2 discharge at 27 mbar.

lower estimate of the field. After the FIW front, the field is directed mainly along the discharge gap, showing a good correlation between the CP and the BCS data. This agreement of E/N by the two techniques is clearly seen as well during the second and the third pulse in figures 3(b) and 3(c). In those pulses, the discharge develops without a sharp peak of E/N due to the high value of residual ionization between the pulses [29].

Synchronized waveforms of the reduced electric field E/N, transmitted current I_{tr} and deposited energy W for the first pulse are presented in figure 4. The deposited energy is 8.2 mJ and most of the energy is deposited during the period of current flowing through the discharge tube. The specific deposited energy ω is correspondingly 0.48 eV/molecule. Will note that the origin of time in this work is set to be at the moment when the FIW closes the discharge gap, i.e. the start of transmitted current.

3.1.2. Initial distribution of electron density: derived from emission measurements of $N_2(C^3\Pi_u) \rightarrow N_2(B^3\Pi_g)$ *transition.* In the first nanoseconds after the ionization wave crossing the gap, the radial profile of electron density is related to the radial profile of radiation intensity of the second positive system (SPS) of nitrogen ($N_2(C^3\Pi_u, v' = 0) \rightarrow N_2(B^3\Pi_g, v'' = 0)$ transition) provided that two conditions are fulfilled: first, the emitting $N_2(C^3\Pi_u)$ state should be populated by electron impact from the ground state $N_2(X^1\Sigma_g^+)$; second, the quenching rate of $N_2(C^3\Pi_u)$ should be independent on the radial coordinate. The second condition is satisfied when the main quenching of $N_2(C^3\Pi_u)$ occurs in the collisions with nitrogen and oxygen molecules and is not correct when the

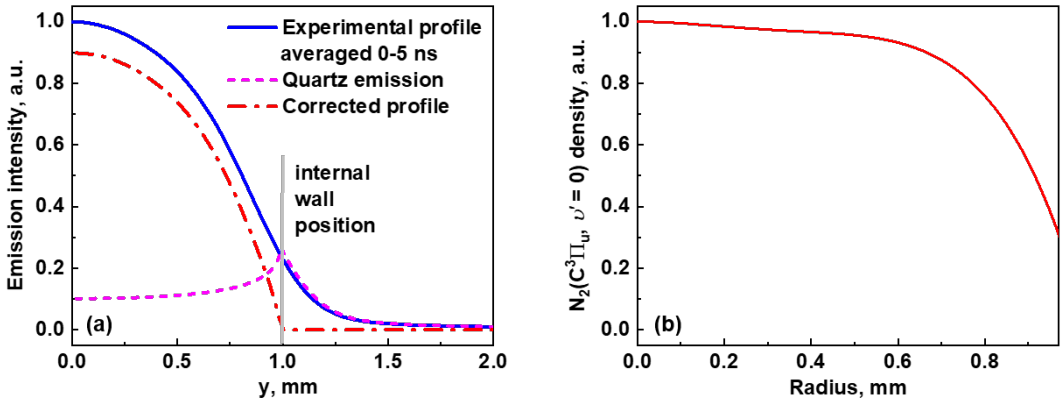

Figure 5. (a) Normalized experimental profile of the emission of the SPS of nitrogen averaging the first 5 ns of the discharge, N_2 + 10% O_2 mixture at 27 mbar. The dashed red profile is the correction using a manually defined distribution of emission caused by light scattering in the quartz wall. (b) Normalized radial distribution of the $N_2(C^3\Pi_u, v'=0)$ density for the corrected emission profile.

quenching by electrons becomes dominant [29]. Under considered conditions, quenching of $N_2(C^3\Pi_u)$ by electrons starts to be noticeable at $n_e \sim 10^{15}$ cm^{-3}, which corresponds to approximately 8-10 ns from the start of the discharge current.

In this work, the emission of SPS of nitrogen $\mathcal{F}(y)$ along the radial axis y of the discharge tube was captured using the ICCD camera (PI-MAX 4 1024i, Princeton Instruments) with the help of a long-distance microscope (QM1, LaVision). Since it is a line-integral measurement, the reverse Abel transform is introduced. Assume that the distribution of the emitting molecules $f(r)$ is axisymmetric and can be presented as a polynomial of order n of the radius r:

$$f(r) = a_0 + a_1 r + a_2 r^2 + \cdots + a_n r^n. \tag{12}$$

where $r \in [0, R_0]$, R_0 is the radius of the plasma channel. Then the Abel transform of this polynomial can be expressed as

$$\mathcal{F}(y) = 2\int_y^{R_0} \frac{(a_0 + a_1 r + a_2 r^2 + \cdots + a_n r^n)\cdot r dr}{\sqrt{r^2 - y^2}} = 2\sum_{i=0}^{n} a_i I_i(y), \tag{13}$$

where the integral functions $I_i(y)_{i\in\{1,2,\ldots,n\}}$ are given by

$$I_i(y) = \int_y^{R_0} \frac{r^{i+1} dr}{\sqrt{r^2 - y^2}}. \tag{14}$$

For every i, $I_i(y)$ depends only on the geometry of the plasma channel, therefore can be expressed analytically and precalculated using the Wolfram Alpha engine [34]. This provides the possibility of using the integrals as basic functions for the decomposition of

$\mathcal{F}(y)$, i.e. experimental profile, in the series over $I_i(y)$ by the least-squares method [35].

An image of the capillary tube illuminated by an LED lamp was acquired to identify the pixels corresponding to the outside boundaries r_{ext} of the tube. The pixels corresponding to the internal walls R_0 of the tube were determined from external boundary coordinates and the known geometry of the tube. A noticeable level of stray emission from the quartz wall of the capillary, $R_0 < r < r_{ext}$, was observed during all the measurements. The following empirical equation was suggested to describe the radial distribution of the wall emission:

$$I_{quartz}(r) = A_1 \cdot \theta(r - R_0) \cdot \theta(r_{ext} - r) \cdot (e^{\frac{-|r-R_0|}{\alpha}} + A_2 e^{\frac{-|r-r_{ext}|}{\alpha}}), \tag{15}$$

where A_1 is the amplitude of scattered light at $r = R_0$, $\theta(r - R_0)$ is a Heaviside step function defined as $\theta = 0$ at $r < R_0$ and $\theta = 1$ at $r \geq R_0$. A_2 is the weight coefficient for the second exponential decay and the decay rate α was selected from the measured emission intensity in the quartz wall. The direct Abel transform of equation (15) was then subtracted from the experimental profile to get the final corrected emission profile, given an example in figure 5(a). In addition, the experimentally normalized emission profile was observed to be approximately the same (within 2%) during the first 5 ns, which proved the independence of the quenching rate of $N_2(C^3\Pi_u)$ state on the radial coordinate. Figure 5(b) shows the obtained radial distribution of $N_2(C^3\Pi_u)$ state emission in $N_2 + 10\%$ O_2 mixture at 27 mbar, which was used as the initial radial distribution of electron density in 1D numerical calculations.

3.1.3. Temperature measurement in the discharge and afterglow. The emission spectrum of the SPS of molecular nitrogen was used for determining the rotational temperature in the discharge and afterglow. The relationship between the rotational temperature of the excited species and the gas temperature depends on the ratio of the lifetimes of the emitting state t_0 and the characteristic time of rotational-translational relaxation t_{RT}. If $t_0 \gg t_{RT}$ (the first case), the emitting molecule is in the thermodynamic equilibrium with surrounding gas and the measured rotational temperature T_{rot}^C is equal to the gas temperature T_g. The second case corresponds to $t_0 \ll t_{RT}$, which means that the influence of a few collisions during the $N_2(C^3\Pi_u)$ lifetime does not perturb the initial Boltzmann rotational distribution formed by direct population by the electron impact from the ground state $N_2(X^1\Sigma_g^+)$. If so, the rotational distribution of the excited state copies the rotational distribution of the ground state [36] according to the Franck-Condon principle. The ground state rotational temperature T_{rot}^X is equal to the translational temperature and the gas temperature can be calculated as:

$$T_g = T_{rot}^X = (B_e^X / B_e^C) T_{rot}^C, \tag{16}$$

where $B_e^X / B_e^C = 1.998/1.825 = 1.095$ [37] is the ratio between the rotational constants of the $N_2(X^1\Sigma_g^+)$ and $N_2(C^3\Pi_u)$ states, T_{rot}^C is the rotational temperature of the

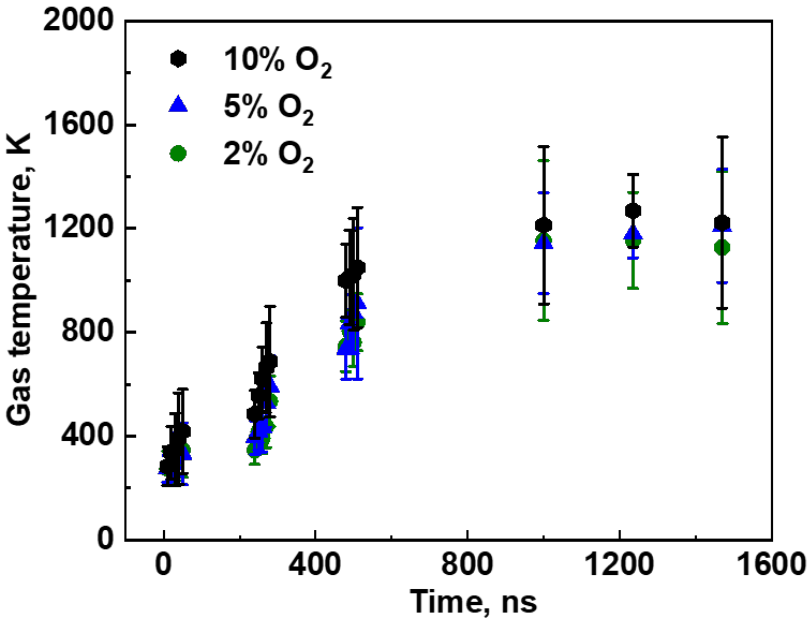

Figure 6. Time evolution of the gas temperature in the nanosecond capillary discharge and near afterglow for different N_2: O_2 mixtures at 27 mbar.

$N_2(C^3\Pi_u)$ state.

It has to be mentioned that the $N_2(C^3\Pi_u)$ state is populated directly from the ground state only at high reduced electric fields, e.g. $E/N > 100$ Td. However, the population of the $N_2(C^3\Pi_u)$ state from the $N_2(B^3\Pi_g)$ state can be significant if $E/N < 100$ Td and the density of the $N_2(B^3\Pi_g)$ state is rather high [38]. In that case, the $N_2(B^3\Pi_g)$ state is in thermal equilibrium with the background gas due to the long lifetime, giving the gas temperature as:

$$T_g = T_{rot}^B = (B_e^B/B_e^C)T_{rot}^C, \tag{17}$$

where $B_e^B/B_e^C = 1.637/1.825 = 0.897$ [37] is the ratio between the rotational constants of the $N_2(B^3\Pi_g)$ and $N_2(C^3\Pi_u)$ states, respectively.

The rotational temperature of the $N_2(C^3\Pi_u)$ state T_{rot}^C was determined by fitting the experimentally measured spectrum using SpecAir software [39]. It was shown in [29, 30] that for similar nanosecond capillary discharge, there are not enough collisions to thermalize the rotational distribution of $N_2(C^3\Pi_u)$ with the background gas. Furthermore, it has been checked that the influence of a few collisions during the $N_2(C^3\Pi_u)$ lifetime under the present conditions does not perturb the initial Boltzmann rotational distribution from the ground state [30]. Thus, for the main three pulses with high electric field, equation (16) was used for the conversion. For the pulses which were the reflections of

the transmitted current pulses from the zero load on the end of the low voltage cable (after 1 μs), the reduced electric field was rather low. With a low oxygen mixture ratio, equation (17) was applied.

The temporal profile of the gas temperature is shown in figure 6. The gas heating in all the N_2: O_2 mixtures at 27 mbar was rather intense: the measured gas temperature increases from 300 K to 1000 K within the first 500 ns, which gives a heating rate of 1400 K $\cdot$ μs^{-1}. Then it gradually reaches the value of 1200 K in the postdischarge period. Will note that this is a usual feature of nanosecond pulsed discharges at high electric fields [40], and the rate of the heating is explained by fast energy relaxation from electronically excited atoms and molecules. According to equation (10), the variance of T_g from 300 K to 1200 K provides the population fraction $f_{J=2}$ from 0.6066 to 0.5994, making it indispensable to be considered in the following TALIF measurements.

3.2. O-atom density measurements

3.2.1. Selection of laser intensity for non-saturated measurements and quenching for atomic Xe and O. By the definition of equations (5) and (6), a linear relationship between the measured TALIF signal and the number density of the species of interest is valid only if the signal demonstrates a quadratic dependence with the laser intensity. Additional processes such as stimulated emission, photoionization and photodissociation are normally neglected compared to the fluorescence if this non-saturated linear regime establishes [12].

To ensure that all the measurements were taken within the non-saturated regime, full spectral scans were taken at various levels of laser intensity. The intensities captured by the photodiode were temporally integrated, squared and maintained at the same level for each wavelength scan. Plotting the temporally and spectrally integrated TALIF signal S versus the quadratic laser intensity, linear relationships were observed both for pure Xe and different ratios of N_2: O_2 mixtures as shown in figures 7(a) and 7(b), respectively. The saturation effect for Xe-TALIF is distinct when the applied laser energy is too high. Based on the linear regime, the laser energy chosen for the following Xe calibration was about 130 μJ and for O-atom density measurements was about 250 μJ.

To determine the effective decay rate $A_{Xe} + Q_{Xe}$ of Xe-TALIF signal, temporal profile $S_t(t)$ taken by PMT was registered and fitted with an exponential decay function $y(t) = e^{-t/\tau}$. The Stern–Volmer plot, Xe-TALIF decay rate versus Xe pressure, was shown in figure 8(a). One can observe a good agreement between the experimental data and the values given in [13], which verifies the feasibility and accuracy of the calibration.

The effective decay rate of O-TALIF signal $A_O + Q_O$ is vital and challenging to

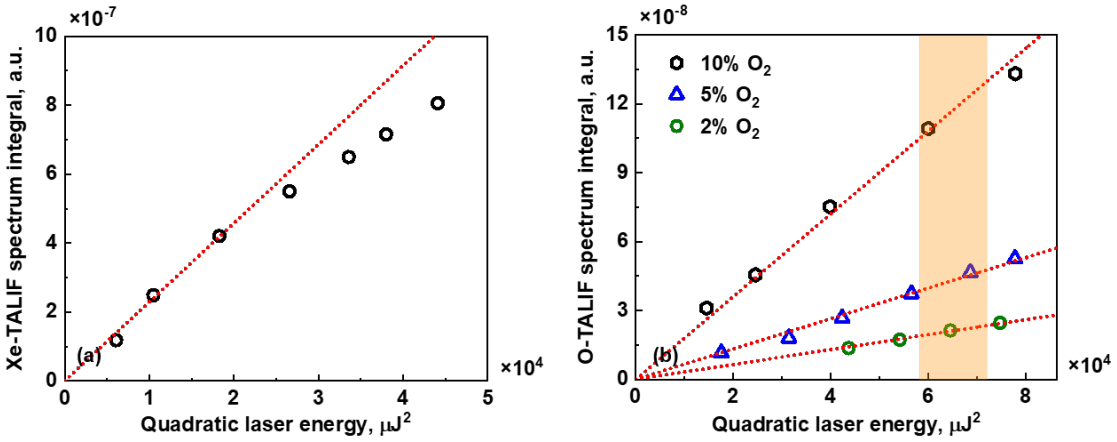

Figure 7. The dependence of (a) Xe-TALIF spectrum integral on the quadratic laser intensity in Xe at 3 mbar. (b) O-TALIF spectrum integral on quadratic laser intensity in different N_2: O_2 mixtures at 27 mbar and laser delay of 5 μs to the discharge. The highlighted part is the range of laser intensities used in the following experiments.

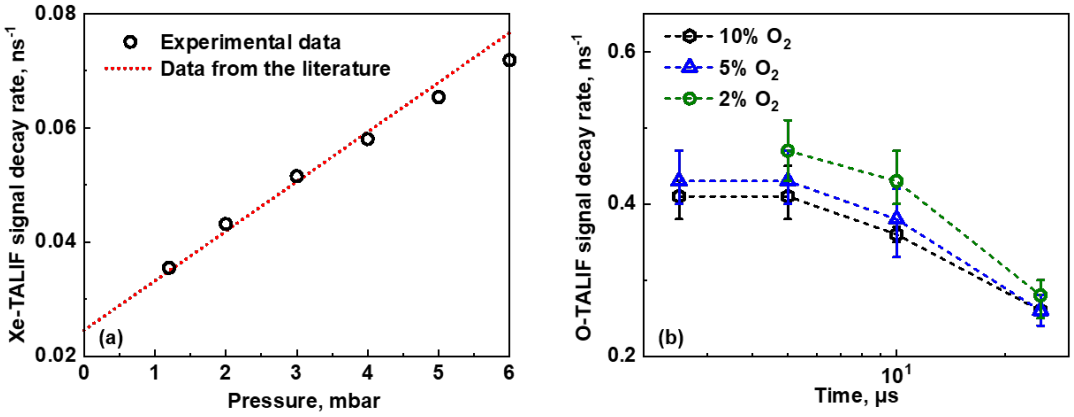

Figure 8. (a) Stern–Volmer (SV) plots of Xe from the experiment and [13] (τ_0^{Xe} = 40.8 ns, $k_{Xe}^{Xe} = 3.6 \times 10^{-10}$ cm^3/s). (b) Time evolution of the O-TALIF signal decay rate for different N_2: O_2 mixtures at 27 mbar.

obtain since the quenching of the excited O-atom in N_2: O_2 mixture is so strong that the decay becomes fast enough to be comparable with the laser pulse duration. The temporal profile $S_t(t)$, which is the convolution of an exponential decay function $y(t)$, the squared laser pulse shape $I^2(t)$ and the instrumental response function $P(t)$ (the shape of the electrical signal observed when the PMT is exposed to an infinitely short light pulse) [41], is more possible to be dominated by the laser profile (6.5 ns pulse duration) rather than the exponential decay. In this case, an optical pulse slicer was employed to shorten the laser pulse duration as shown in figure 1(b). It is a combination of a Pockels cell and a polarizer. Applying a high voltage across the cell alters the bire-

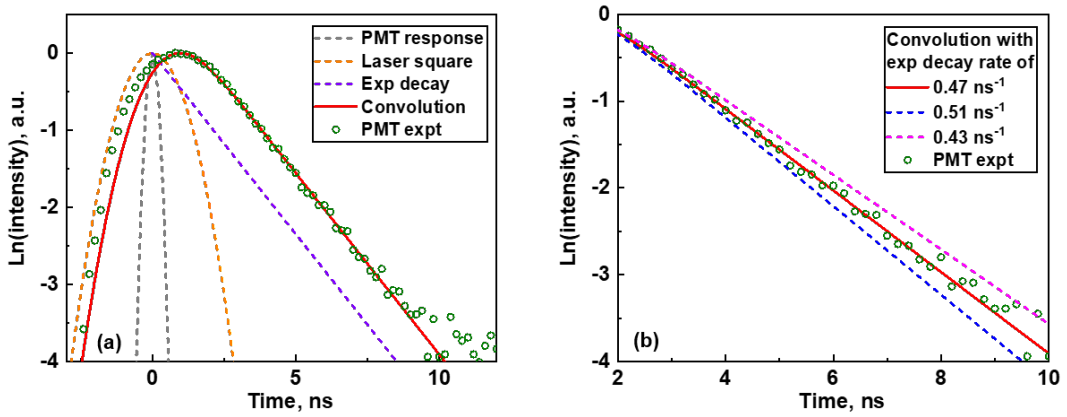

Figure 9. (a) Example of decay rate fitting for O-TALIF signal, including temporal profiles of PMT response, laser pulse, exponential decay, convolution result and experimental data for N_2 + 2% O_2 at 27 mbar with the delay time of 5 μs. (b) Example of error estimation of the decay rate fitting.

fringence of the cell material, and thereby rotates the polarization of the light passing through. The polarization response occurs instantaneously and lasts for as long as the high voltage is sustained across the cell [42, 43]. The Pockels cell used in this work is developed by Leysop Ltd and consists of a UV BBO crystal mounted in a housing with electrical leads. It is driven by a FID high voltage generator (FDS 3-1NM1), delivering up to 3 kV pulses with a nominal width of 2.5 ns (FWHM). These pulses are terminated with a matching 50 Ω high voltage load. As a result, the FWHM of the UV beam after the pulse slicer is shortened from 6.5 ns to 2.5 ns.

A de-convolution process was then performed: by changing the time coefficient of the exponential decay function, one can get the best convolution result fitted to the experimental data with the least root mean square error (RMSE). Figure 9(a) gives an example of the fitting result and the corresponding error range determination is shown in figure 9(b). Finally, figure 8(b) shows the O-TALIF signal decay rates along with time for all N_2: O_2 mixtures.

3.2.2. O-atom density measured in three mixtures with different percentages of O_2. According to equation (11), O-atom density is determined by a series of parameters, whose values are listed in table 1. The two-photon absorption cross-section ratio $\sigma^{(2)}_{Xe}/\sigma^{(2)}_{O}$ (predefined), natural lifetime of the excited τ_0^{Xe} and τ_0^{O} were taken from the literature [13]. The number density n_{Xe} and decay rate $A_{Xe} + Q_{Xe}$ were calculated based on the Xe calibration at 300 K, 3 mbar. The decay rate of excited O-atom $A_O + Q_O$ was taken from the experimental data as shown in figure 8(c). Transmission of the bandpass filter F was measured by the Cary 60 UV-Vis spectrophotometer at the wavelength interval between 820 nm to 880 nm. The quantum efficiency of PMT η at different fluorescence

Table 1. Parameter values applied for O-atom quantification.

Parameter	Value	Unit	Reference
n_{Xe}	7.4×10^{16}	cm^{-3}	this work
$\sigma_{Xe}^{(2)}/\sigma_{O}^{(2)}$	1.9	–	[13]
ν_O^2/ν_{Xe}^2	0.9882	–	[13]
$A_{Xe} = 1/\tau_0^{Xe}$	1/40.8	ns^{-1}	[13]
$A_O = 1/\tau_0^{O}$	1/34.7	ns^{-1}	[13]
$A_{Xe} + Q_{Xe}$	0.05	ns^{-1}	this work
F_{Xe}/F_O	1.0096	–	this work
η_{Xe}/η_O	1.36	–	this work
$f_{J=2}$	0.6066	–	this work

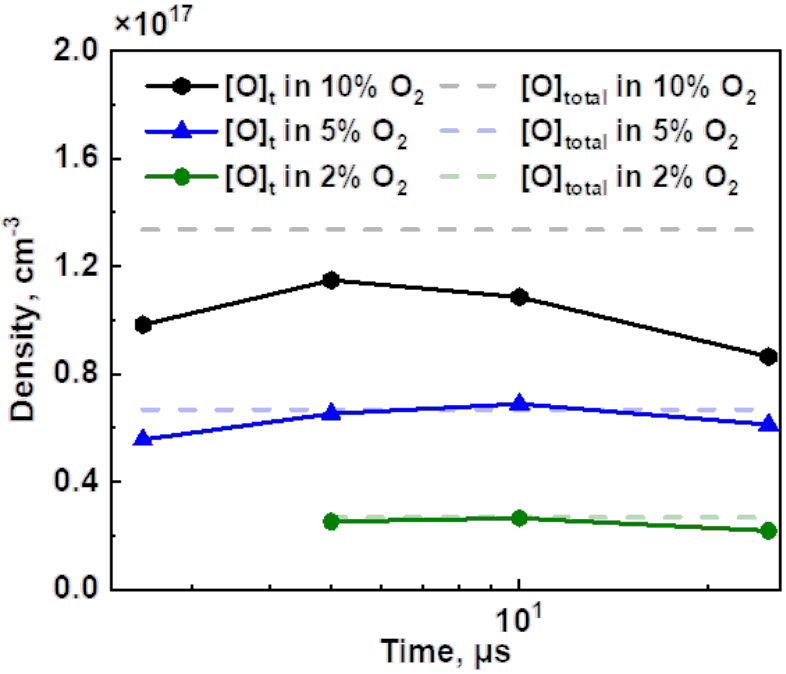

Figure 10. Time evolution of the O-atom absolute density in different N_2: O_2 mixtures at 27 mbar. The dashed lines are the total O-atom densities when complete dissociation is satisfied. The cross-section ratio $\sigma_{Xe}^{(2)}/\sigma_{O}^{(2)}$ is predefined as 1.9 taken from [13].

wavelengths for atomic Xe and O was obtained experimentally using a halogen light source (Ocean Insight HL-2000) and a spectrometer (Andor SR-500i-B1) with a calibrated diffraction grating. $f_{J=2}$ was taken from equation (10) using the gas temperature of 1200 K measured in section 3.1.3. The variance of T_g was proved to be minor during the period of 2.5 μs to 25 μs by analyzing the FWHM of fluorescence spectrum at each time delay.

As a result, time evolutions of O-atom density in different N_2: O_2 mixtures at

27 mbar were calculated and shown in figure 10. The dashed line expresses the total O-atom density in the corresponding mixture when a condition of the complete dissociation is satisfied. For the time period from 2.5 μs to 25 μs, all the O_2 were dissociated to O-atom in the mixture of $N_2 + 5\%$ O_2 and $N_2 + 2\%$ O_2 based on the TALIF measurements. For the case of $N_2 + 10\%$ O_2, the dissociation degree is approximately 70%.

4. Numerical approach

As it is discussed above, the used technique for absolute calibration of the ratio of Xe/O two-photon absorption cross-sections is based on the statement of complete dissociation of oxygen molecules in the discharge. To verify this statement and to analyze the main channels of O_2 dissociation, numerical simulation of the discharge parameters was performed for conditions of the present experiment.

The calculations were carried out in 1D approximation describing the temporal evolution of radial profiles of particle density at axial symmetry. The validity of suggested approximation is proved by the fact that radial gradients of the discharge parameters are much higher than the axial gradients in the interelectrode direction. The longitudinal electric field E was calculated as

$$E = \frac{I}{2\pi e \int\limits_0^R n_e(r)\mu_e(r) r dr}, \tag{18}$$

where $n_e(r)$ and $\mu_e(r)$ are the radial profiles of electron density and electron mobility, $R = 1$ mm is the internal radius of the discharge tube.

The numerical modeling focuses on the detailed kinetics in N_2: O_2 mixtures after the closing of the discharge gap by FIW and in the near afterglow. The initial radial profile of electron density $n_e(r)$, and the temporal evolution of the conductive current I, both measured experimentally, were taken as the input data of the code. The gas density was assumed to be constant since the time scale of considered processes (< 3 μs) is much less than a characteristic time of the gas extension ($\sim$ 20-30 μs for characteristic dimensions of the discharge cell).

The following equation was solved for the electron density:

$$\frac{\partial n_e}{\partial t} = \frac{1}{r}\frac{\partial}{\partial r}\left(r D_a \frac{\partial n_e}{\partial r}\right) + n_e\left(\nu_{ion} - \nu_{att}\right) - Q_{rec} + Q_{det}, \tag{19}$$

here, D_a is the ambipolar diffusion coefficient, ν_{ion} and ν_{att} are the electron impact ionization and attachment frequencies, Q_{rec} is the electron-ion recombination rate, and the term Q_{det} accounts for all the processes of electron detachment from negative ions in collisions with $O(^3P)$ atoms. The densities of other charged species are determined

from similar balance equations.

Ionization, dissociation and excitation rates were calculated for each time instant as a function of reduced electric field on the basis of the solution of the Boltzmann equation in a two-term approximation using BOLSIG+ code [44] with the imported cross-sections for N_2 molecules [45], for O_2 molecules [46, 47] and for O atoms [48]. To describe the dissociation of $N_2(A^3\Sigma_u^+, B^3\Pi_g, C^3\Pi_u, a'^1\Sigma_u^-)$ molecules by electron impact, the cross sections calculated in [49] were used. Here and below $N_2(B^3\Pi_g)$ will denote combined triplet states $N_2(B^3\Pi_g, B'^3\Sigma_u^-, W^3\Delta_u)$ and $N_2(a'^1\Sigma_u^-)$ - combined singlet states $N_2(a'^1\Sigma_u^-, a^1\Pi_g, w^1\Delta_u)$.

It should be noted that the two-term approximation is valid [45, 50] for the considered experimental conditions because the reduced electric field in the region of the main energy input does not exceed a few hundreds of Td. The *e-e* processes were taken into account in the calculations, since at the end of one of the main pulses at relatively high electron densities and low electric fields, $E/N < 100$ Td, electron–electron collisions become important for EEDF formation, electron drift velocity and rates of excitation for considered electronically excited states.

The main reactions determining the production of atomic nitrogen and oxygen in N_2: O_2 mixtures are given in table 2. The basis of the kinetic model is the reactions described in detail and analyzed in [40,51]. Results of the verifications related to the role of the reactions of nitrogen dissociation by electron impact at conditions of low specific energy deposition (SED) were analyzed in [52]. The role of the reactions of stepwise dissociation of electronically excited states $N_2(A^3\Sigma_u^+, B^3\Pi_g, C^3\Pi_u)$ in discharges with high ionization degree was considered in [53]. In [30], the main processes of fast gas heating in N_2: O_2 plasma at high ionization degrees and high specific energy deposition were discussed. The obtained results were used for the fine-tuning of the kinetic model of a gas-discharge nitrogen-oxygen plasma, which is particularly important for the present conditions.

5. Discussion of the calculation results

As mentioned in section 4, experimentally obtained waveforms of electrical current were used as input data in the calculations (see figure 4). An example of the modeling of plasma parameters for the first discharge pulse is presented in figure 11(a). The calculations were made for N_2 + 5% O_2 mixture for initial pressure and gas temperature $P_0 = 27$ mbar and $T_0 = 300$ K respectively. Good agreement between the temporal behavior measured by the capacitive detector (curve 1) and calculated (curve 2) reduced electric field $E/N(t)$ is clearly seen. Calculated averaged over the cross-section specific deposited energy (curve 3) provides the same value as experimentally measured one (a point). Most of the discharge energy is deposited in the gas at E/N = 150–300 Td,

Table 2. The main reactions determining the production of nitrogen and oxygen atoms in N_2: O_2 mixtures used in the model.

No.	Reaction	Rate constant, cm^3s^{-1}	Reference
C1	$O_2^+ + e \rightarrow O(^3P,^1D) + O(^1D)$	$2 \times 10^{-7} \times (300/T_e)^{0.7}$	[54]
C2	$N_2^+ + e \rightarrow N(^4S) + N(^2D)$	$2 \times 10^{-7} \times (300/T_e)^{0.37}$	[54]
C3	$O_2 + e \rightarrow O(^3P,^1D) + O(^3P) + e$	$f(E/N)$	[46,47]
C4	$N_2 + e \rightarrow N(^4S) + N(^2D) + e$	$f(E/N)$	[52,55]
C5	$N_2(A^3\Sigma_u^+, B^3\Pi_g, C^3\Pi_u) + e \rightarrow N(^4S) + N(^2D) + e$	$f(E/N)$	[49,53]
C6	$N_2(A^3\Sigma_u^+) + O_2 \rightarrow O(^3P) + O(^3P) + N_2$	2.5×10^{-12}	[40,51,56]
C7	$N_2(B^3\Pi_g) + O_2 \rightarrow O(^3P) + O(^3P) + N_2$	3.0×10^{-10}	[40,51,56]
C8	$N_2(a'^1\Sigma_u^-) + O_2 \rightarrow O(^3P) + O(^1D) + N_2$	2.8×10^{-11}	[40,51,56]
C9	$N_2(C^3\Pi_u) + O_2 \rightarrow O(^3P) + O(^1D) + N_2$	3.0×10^{-10}	[40,51,56]
C10	$N_2(B^3\Pi_g, a'^1\Sigma_u^-, C^3\Pi_u) + O(^3P) \rightarrow NO + N(^2D)$	3.0×10^{-10}	[57]
C11	$N(^2D) + O_2 \rightarrow NO(v) + O(^3P,^1D)$	$7.5 \times 10^{-12} \times (T/300)^{0.5}$	[56]
C12	$N(^2D) + N_2 \rightarrow N(^4S) + N_2$	$4.52 \times 10^{-14} \times T^{0.68} \times \exp(-1438/T)$	[58]
C13	$N(^4S) + O_2 \rightarrow NO + O(^3P)$	$1.1 \times 10^{-14} \times T \times \exp(-3150/T)$	[40,51,56]
C14	$N(^4S) + NO \rightarrow N_2(v) + O(^3P)$	$1.05 \times 10^{-12} \times T^{0.5}$	[40,51,56]

suggesting a high energy efficiency of dissociation of the mixture molecules.

Similar calculations were performed for the second discharge pulse. The results of the calculations are shown in figure 11(b). The average specific delivered energy in the second pulse is approximately the same as in the first pulse, and most of this energy is deposited in the gas at approximately the same E/N. Agreement between the measurements and calculations in both the first and second pulses proves that the model adequately describes not only ionization but excitation of other degrees of freedom, in particular excitation of electronic states and the dissociation. Will note that high

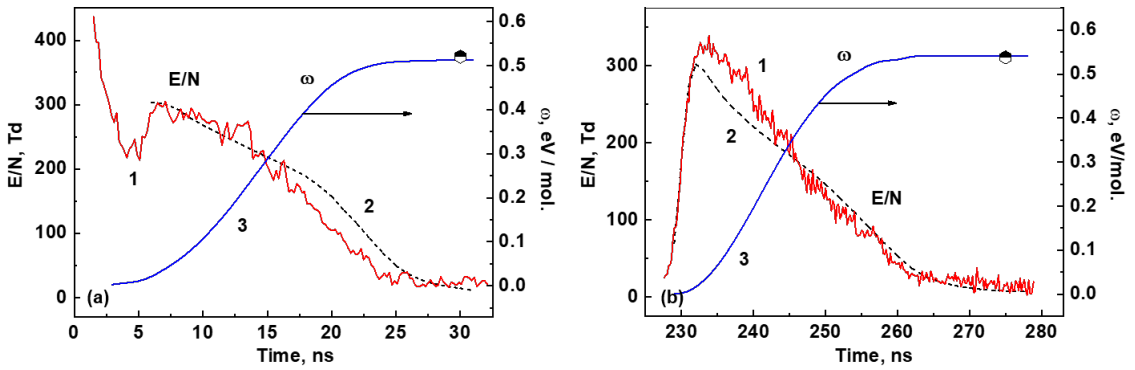

Figure 11. Time behaviour of the reduced electric field E/N and specific energy deposition ω in (a) the first and (b) the second pulse for $N_2 + 5\%$ O_2 mixture at 27 mbar. Curve 1 and the point are the experimental data, curves 2 and 3 are the calculation results.

dissociation degrees of N_2 molecules and high energy efficiency of N-atom generation, $G_N \sim 10$ N-atom/100 eV, were recently obtained in a similar discharge in molecular nitrogen [53].

The results of comparison of the calculated data on specific energy deposition for all three discharge pulses with the measured data in mixtures of N_2 + 5% O_2 and N_2 + 10% O_2 are given in table 3. It should be noted that the SED values in the nanosecond capillary discharge are quite high: the average specific deposited energy over the discharge cross-section $\omega > 1$ eV/mol, and in the near-axis region of the discharge the energy is about 1.5 times higher.

Table 3. Comparison of experimental and calculated average specific energy deposition (SED) in three discharge pulses for $N_2 + 5\%$ O_2 and $N_2 + 10\%$ O_2 mixtures.

Pulse	ω, eV/mol.			
number	expt, 5% O_2	**calc, 5% O_2**	expt, 10% O_2	**calc, 10% O_2**
1	0.52	**0.51**	0.48	**0.48**
2	0.53	**0.54**	0.56	**0.52**
3	0.093	**0.13**	0.11	**0.11**
Sum	1.15	**1.18**	1.15	**1.12**

The kinetic curves of the main components during three discharge pulses and in the afterglow for different percentages of oxygen in the mixture are shown in figure 12. A common feature for 10% (figure 12(a)), 5% (figure 12(b)) and 2% (figure 12(c)) of O_2 in nitrogen is that the electron density reaches $\sim 10^{15}$ cm^{-3} already in the first pulse. Three peaks of the electron density in time correspond to three discharge pulses separated by 250 ns. A sharp increase of O-atom density is observed for each pulse; [O] continues increasing between the pulses, and finally, smooth growth of atomic oxygen concentration continues in the afterglow on submicrosecond timescale. For all three mixtures considered, the results of O-atom density calculations agree with the measured data (points). The decrease in the experimental atomic density at times t > 20 μs can be attributed to gas-dynamic extension due to the arrival of a rarefaction wave in the considered section of the discharge channel, which was not taken into account in the model.

In order to analyze the main reactions leading to the production of atomic oxygen, a comparative analysis of the rates of the reactions giving the greatest contribution to the formation of O atoms was carried out. The results of the calculations are presented in figure 13. During the discharge pulses and early afterglow between them (0 ns $< t <$ 500 ns), the main contribution to the production of O atoms comes from the reactions of dissociative quenching of excited nitrogen molecules by O_2 (reactions C6-C9 in table 2 and in figure 13):

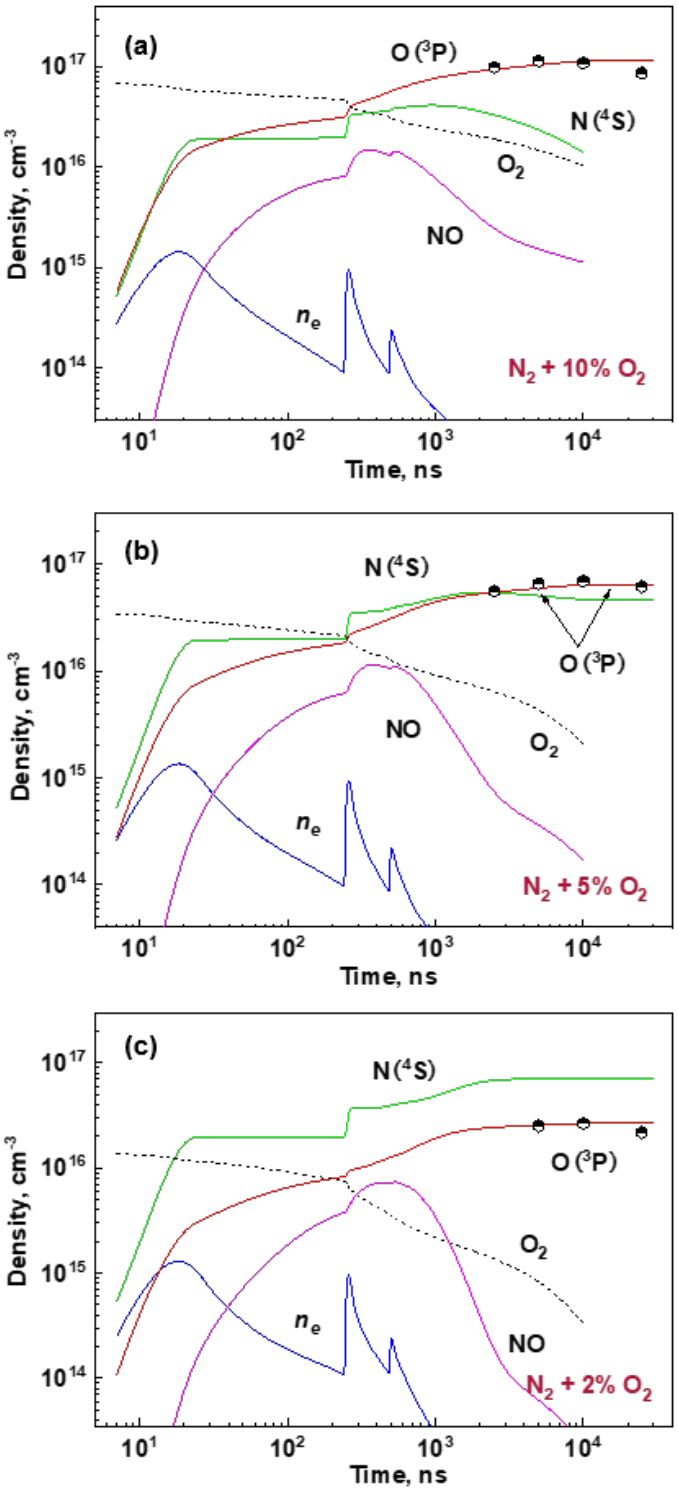

Figure 12. Time evolution of main species densities near the discharge axis, calculated with 1D kinetic model in (a) N_2 + 10% O_2 (b) N_2 + 5% O_2 (c) N_2 + 2% O_2 at 27 mbar. Points are experimental data (see figure 10), curves are the results of calculation.

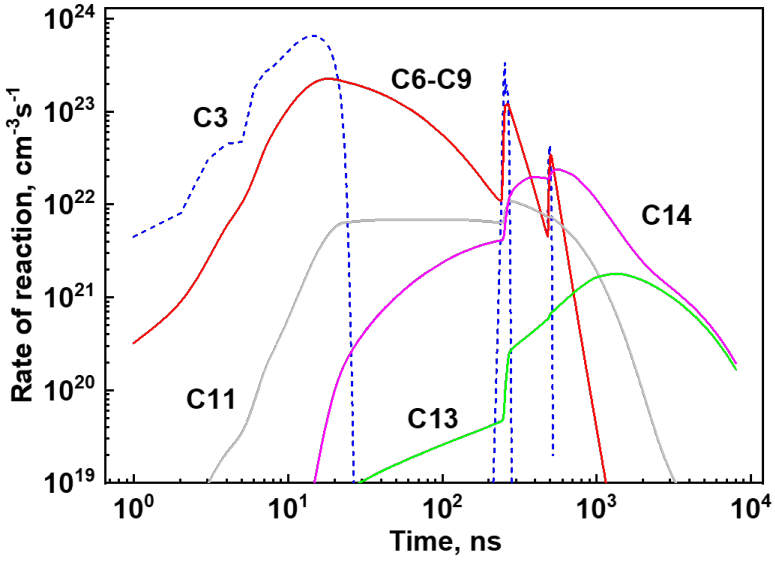

Figure 13. The rate of reaction for O-atom production at the discharge axis in the $N_2+5\%$ O_2 mixture: C3. $O_2+e \rightarrow 2O+e$, C6 – C9. $N_2(A^3\Sigma_u^+, B^3\Pi_g, a'^1\Sigma_u^-, C^3\Pi_u)+O_2 \rightarrow 2O+N_2$, C11. $N(^2D)+O_2 \rightarrow NO+O$, C13. $N(^4S)+NO \rightarrow N_2+O$, C14. $N(^4S)+O_2 \rightarrow NO+O$.

$$N_2(A^3\Sigma_u^+, B^3\Pi_g, a'^1\Sigma_u^-, C^3\Pi_u) + O_2 \rightarrow O(^3P) + O(^3P,^1D) + N_2. \quad (20)$$

The concentration of molecular oxygen in the time interval 0 ns $< t <$ 250 ns drops significantly. As the [O]/[O_2] ratio increases, the role of the pathway (reactions C7-C9) decreases because electronically excited $N_2(B^3\Pi_g, a'^1\Sigma_u^-, C^3\Pi_u)$ molecules are quenched by atomic oxygen (reaction C10 in table 2):

$$N_2(B^3\Pi_g, a'^1\Sigma_u^-, C^3\Pi_u) + O(^3P) \rightarrow NO + N(^2D). \quad (21)$$

To understand the main pathways in the afterglow, at $t > 600$ ns, will consider first the dissociation of $N_2(A^3\Sigma_u^+, B^3\Pi_g, C^3\Pi_u)$ in the discharge. The main source of N-atoms [53] is the dissociation by direct electron impact (reaction C5 in table 2):

$$N_2(A^3\Sigma_u^+, B^3\Pi_g, C^3\Pi_u) + e \rightarrow N(^4S) + N(^2D) + e. \quad (22)$$

Obtained N-atoms, in the ground $N(^4S)$ and excited $N(^2D)$ states, produce atomic oxygen in the following collisions with oxygen or NO molecules in reactions C11, C13 and C14 in table 2:

$$N(^2D) + O_2 \rightarrow NO(v) + O(^3P,^1D), \quad (23)$$

$$N(^4S) + O_2 \rightarrow NO + O(^3P), \quad (24)$$

$$N(^4S) + NO \rightarrow N_2(v) + O(^3P). \quad (25)$$

Reaction C14 produces the maximum amount of atomic oxygen in the afterglow. The rate of reaction C11 drops sharply in the afterglow due to the quenching of excited nitrogen $N(^2D)$ atoms by nitrogen molecules, reaction C12:

$$N(^2D) + N_2 \rightarrow N(^4S) + N_2. \quad (26)$$

Indeed, the rate constant of the reaction C12 increases significantly with gas temperature [58]. Up to 90% of the excitation energy of $N(^2D)$ atoms in this reaction goes into the heating of the gas and only less than 10% into the vibrational excitation of $N_2(v)$.

In the developed kinetic model, the rates of several important reactions strongly depend on the gas temperature. These are the reactions of quenching of $N(^2D)$ atoms by nitrogen (C12) [58] and oxidation of atomic nitrogen $N(^4S) + O_2 \rightarrow NO + O(^3P)$ (C13) [56]. Figure 14 shows the results of calculations (curves) and measurement data (points) of the temporal behavior of the gas temperature in the considered discharge and near afterglow. The dashed curve corresponds to the gas temperature on the discharge axis, and the solid curve corresponds to the temperature averaged over the discharge cross-section (see [30]). As can be seen, the developed model allows an adequate description of the experimental data on gas heating and, accordingly, of the values of rate constants with a strong temperature dependence. The fraction of the discharge energy going to 2 μs into gas heating is $\eta_R = 23\%$, which is comparable to the efficiency of fast gas heating (FGH) under similar conditions in nitrogen and air [30]. In the post-discharge period, the gas cools down due to the thermal conductivity: at $P = 27$ mbar and tube radius $R = 1$ mm, the time of temperature decrease to 900 K is 30–40 μs.

To analyze the spatial distribution of the dissociation degree of oxygen molecules, the radial profiles of $O(^3P)$ atoms at different time moments were calculated. At relatively high electron density in the capillary discharge ($n_e \sim 10^{15}$ cm^{-3}), electron-ion recombination reactions cause the radial profiles of n_e(r) significantly flatter during the pause between discharge pulses (higher recombination rate in the center and lower at the periphery). From pulse to pulse and with time, the distribution becomes more and more flat, causing a similar flat O-atoms distribution. Figure 15 shows examples of such calculations for N_2: O_2 mixtures at time t = 20 μs after discharge initiation. The densities are presented in linear scale and normalized to absolute values of a maximum over the cross-section O-atoms density, $[O]_{max}$, for each profile. As can be seen, for mixtures with oxygen fractions of 2% and 5%, the $[O](r)/[O](r = 0)$ ratio exceeds 90% at $r < 0.85$ mm and $r < 0.75$ mm, respectively.

The results of the calculations and their comparison with the experimental data show that the assumption of complete dissociation of oxygen molecules in this discharge

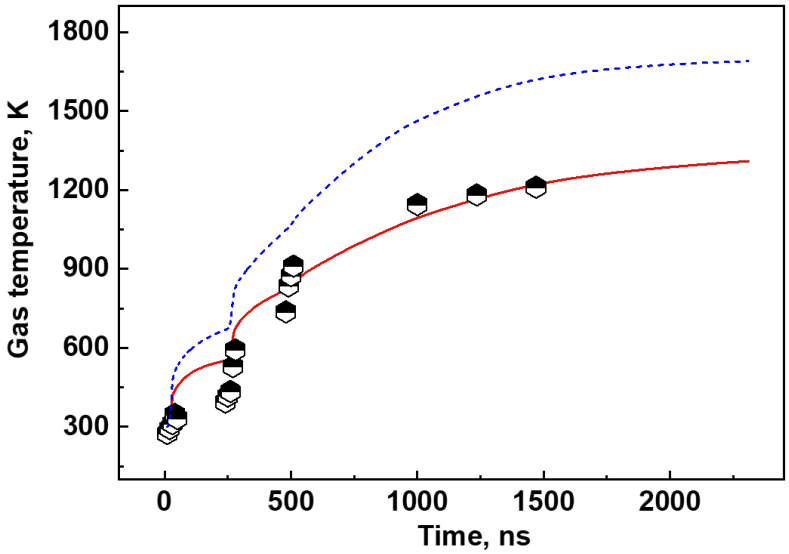

Figure 14. Temporal dynamics of gas temperature for N_2 + 5% O_2 mixture at 27 mbar. Points are experimental data (see figure 6), curves are calculation results: the dashed curve - at the discharge axis, the solid curve - averaged over the cross-section.

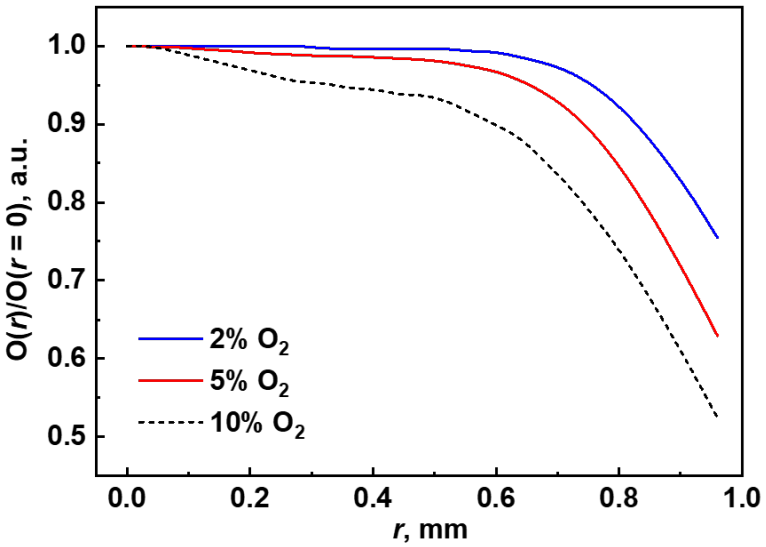

Figure 15. Normalized radial densities of atomic oxygen $O(r)/O(r = 0)$ at 20 μs after discharge in different mixtures: $[O]_{max} = 2.73 \times 10^{16}$ cm^{-3} for N_2 + 2% O_2, $[O]_{max} = 6.8 \times 10^{16}$ cm^{-3} for N_2 + 5% O_2 and $[O]_{max} = 1.28 \times 10^{17}$ cm^{-3} for N_2 + 10% O_2.

is fulfilled for N_2: O_2 mixtures with oxygen fraction less than 6–7%. This fact is used to determine the ratio of Xe/O two-photon absorption cross-sections within the framework

Table 4. Calculation results of Xe/O two-photon absorption cross-section ratio in $N_2 + 5\%$ O_2 and $N_2 + 2\%$ O_2 mixtures.

O_2 fraction, %	Time, μs	α, a.u.	$\sigma^{(2)}_{Xe}/\sigma^{(2)}_{O}$, a.u.	Uncertainty, %
5	5	0.91	1.77	11.05
5	10	0.91	1.67	11.36
5	25	0.91	1.88	10.82
2	5	0.95	1.83	11.70
2	10	0.95	1.82	11.40
2	25	0.95	2.13	12.73

of the technique presented in section 3.2.

Therefore, at the known density of O-atoms in a nanosecond capillary plasma, the ratio of the two-photon absorption cross-sections $\sigma^{(2)}_{Xe}/\sigma^{(2)}_{O}$ was determined experimentally according to equation (11):

$$\frac{\sigma^{(2)}_{Xe}}{\sigma^{(2)}_{O}} = \alpha \cdot \frac{n^{ref}_{O}}{n_{Xe}} \cdot \frac{\nu^2_{Xe}}{\nu^2_{O}} \cdot \frac{A_O}{0.733 \cdot A_{Xe}} \cdot \frac{A_{Xe} + Q_{Xe}}{A_O + Q_O} \cdot \frac{F_O}{F_{Xe}} \cdot \frac{\eta_O}{\eta_{Xe}} \cdot \frac{S_{Xe}/I^2_{Xe}}{S_O/I^2_O} \cdot f_{J=2}, \qquad (27)$$

where α is the correction factor caused by radial distribution of oxygen atoms discussed above and in Appendix, and by laser beam passing through this distribution; n^{ref}_{O} is the "reference" density of oxygen atoms $[O]_{ref}=2\cdot[O_2]_0$, where $[O_2]_0$ is the initial density of oxygen molecules. The values of other parameters are listed above in table 1. Experimental points in N_2 + 5% O_2 and N_2 + 2% O_2 mixtures after 5 μs were selected to calculate the corresponding cross-section ratio. The results are shown in table 4 with detailed accuracy analysis discussed in the Appendix. Data point with a big error at 25 μs in N_2 + 2% O_2, statistically situated out of the data set mainly due to a low signal-to-noise ratio, was excluded from the data treatment. Analysis of the five remaining experimental points, using the Student's statistic [59] for the 95% confidence interval to account for the scatter of the final data and related stochastic error, led to the following result for the cross-section ratio:

$$\sigma^{(2)}_{Xe}/\sigma^{(2)}_{O} = 1.8 \pm 0.2. \qquad (28)$$

6. Conclusions

This paper presents a calibration of the ratio of the two-photon absorption cross sections, $\sigma^{(2)}_{Xe}/\sigma^{(2)}_{O}$, namely $5p^6\ {}^1S_0 \rightarrow 6p'[3/2]_2$, 224.31 nm wavelength for Xe and $2p^4\ {}^3P_2 \rightarrow 3p\ {}^3P_J$, 225.65 nm wavelength for oxygen atom. The calibration is based on TALIF measurements carried out in a specifically designed pulsed nanosecond discharge

that operates at medium pressures and has a predefined concentration of atomic oxygen.

To achieve this objective, a pulsed nanosecond capillary discharge operating at medium pressures, 20-30 mbar, was proposed. In this pressure range, the discharge is stable and well-reproducible. A distinctive feature of this discharge is the high values of total specific delivered energy, $\omega > 1$ eV/mol, and the major part of this energy is released at high electric fields, E/N = 150–250 Td. As a result, the efficiency of dissociation of molecules in plasma is high [17, 29]. In mixtures of nitrogen with small oxygen additives, high values of the dissociation degree of oxygen molecules, up to 100% dissociation of O_2, are observed in the afterglow of the discharge.

Three different mixtures, 10%, 5% and 2% of oxygen in nitrogen, were considered in this work. The gas flow rate at 27 mbar pressure was chosen to ensure that, at a given discharge pulse repetition rate of 10 Hz, the gas was changed between pulses. Each discharge was excited by a burst of three pulses of about 9.4 kV amplitude in the cable, with an FWHM of 35 ns and a time interval of 245 ns between them. Each experiment included measurements of the full set of discharge parameters: voltage at the electrodes, electrical current in the plasma, longitudinal electric field and energy delivered to the gas, all measurements synchronized with 0.2 ns accuracy. Additionally, the radial distribution of emission of excited nitrogen molecules and the gas temperature in the discharge and afterglow were measured.

Atomic oxygen density at $t \geq 1$ μs was measured by TALIF technique. Usually, the knowledge of the ratio of Xe/O two-photon absorption cross-sections, $\sigma^{(2)}_{Xe}/\sigma^{(2)}_{O}$, is necessary to determine absolute density of O atoms. The fact that complete dissociation of oxygen molecules can be achieved in the considered discharge, was used to calculate the ratio $\sigma^{(2)}_{Xe}/\sigma^{(2)}_{O}$. For this purpose, the value $[O]_{ref} = 2 \cdot [O_2]_0$, where $[O_2]_0$ is the initial density of oxygen molecules, was used as a reference value for the density of O atoms.

To verify the assumption of complete dissociation of oxygen molecules and to determine the main channels of O_2 dissociation, 1D axisymmetric calculations [30] were performed taking the measured time profile of the discharge current pulse as initial data. The results of calculation were compared with the measured data on the reduced electric field $E/N(t)$ and the specific energy contribution ω in each of the three pulses in the burst, as well as with the time behavior of gas temperature $T(t)$ in the discharge and near afterglow. The results of calculations agree with the measurement data, indicating the accuracy of the description of all key discharge parameters. This allows the use of the developed model for prognostic assessments.

In the discharge under consideration, the main channels of O-atom production are reactions of quenching of excited states of $N_2(A^3\Sigma^+_u, B^3\Pi_g, C^3\Pi_u, a'^1\Sigma^-_u)$ by oxygen molecules, as well as reactions of atomic nitrogen, in the ground $N(^4S)$ and excited

$N(^2D)$ states, with O_2. Significant contribution of reactions involving atomic nitrogen to the production of O atoms is related to the high density of N atoms, which, in turn, is a consequence of efficient dissociation of $N_2(A^3\Sigma_u^+, B^3\Pi_g, C^3\Pi_u)$ by electron impact [53].

According to the calculated data, the assumption of complete dissociation of oxygen molecules is fulfilled for N_2: O_2 mixtures with oxygen fraction less than 6-7%. Therefore, for these mixtures, comparison of the data obtained by the TALIF technique with the "reference" density of $[O]_{ref}$ atoms, was used to determine the ratio of Xe/O two-photon absorption cross-sections. Special attention was paid to the analysis of laser beam passage through the section of a capillary with weakly inhomogeneous density of atomic oxygen and to the analysis of measurement error. The result of this calibration provides the following value:

$$\sigma^{(2)}_{Xe} / \sum_{J'} \sigma^{(2)}_{O(J\to J')} = 1.8\ (\pm 0.2).$$

The value of $\sigma^{(2)}_{Xe}/\sigma^{(2)}_{O}$ obtained in this work is similar to the data obtained in [13] and differs markedly from the ratio used in [27] were it was suggested, following [25, 26] that the ratio should be reduced by a factor slightly greater than 2. The question of how the ratio of cross sections relates to the absolute value of the cross-section of the two-photon excitation of Xe measured in [25, 26] remains open.

Acknowledgements

This work was partially supported by the Energy4Climate Interdisciplinary Center (E4C) of IP Paris and Ecole des Ponts ParisTech in the framework of the 3rd Programme d'Investissements d'Avenir [ANR-18-EUR-0006-02] and by the private sponsor Résilience des systèmes énergétiques au changement climatique et émissions négatives financed by Engie Foundation. The authors are thankful to Dr. Geoffrey Kreyder for developing a code for ray tracing and to Dr. Inna Orel for fruitful discussions. The work of Dr. Nikolay Popov was partially supported by the Russian Science Foundation, Project No. 23-17-00264. The support for Mr. Zhan Shu by the China Scholarship Council (CSC) program for PhD students is gratefully acknowledged.

Appendix A. Accuracy of the measurements of the ratio of Xe/O two-photon absorption cross-sections

The systematic errors of the measurements mainly come from the inhomogeneous distribution of oxygen atoms over the cross-section of the discharge capillary. Three approaches to the error estimation are described below. For all of them, it was assumed that the laser beam is homogeneous along the propagation direction and passes through the center of the capillary.

In the first simplified approach, refraction of the laser beam when passing through the capillary was neglected, and the interaction of the cylindrical laser beam with the distribution of O atoms in the capillary was considered. Then the average along the beam length density of atoms, O_{av}, can be calculated using the following expression:

$$O_{av} = \frac{1}{Z} \cdot \int_0^Z O(r)dr + \frac{\int_Z^R (R^2 - r^2) \cdot O(r)dr}{\int_Z^R (R^2 - r^2)dr}. \quad (A.1)$$

Here, $Z = \sqrt{R^2 - R_0^2}$, $R = 1$ mm is the radius of the capillary and $R_0 = 0.5$ mm is the radius of the laser beam. The results of calculations provide the difference between the maximum (plateau) value of O-atoms taken in the paper and the averaged according to the formula above [O_{av}]: at $t > 5$ μs, Δ[O] = ([O] − [O_{av}])/[O] = 3-4% for the mixture N_2 + 2% O_2, Δ[O] = 7% for the mixture N_2 + 5% O_2, Δ[O] = 11-12% for the mixture N_2 + 10% O_2.

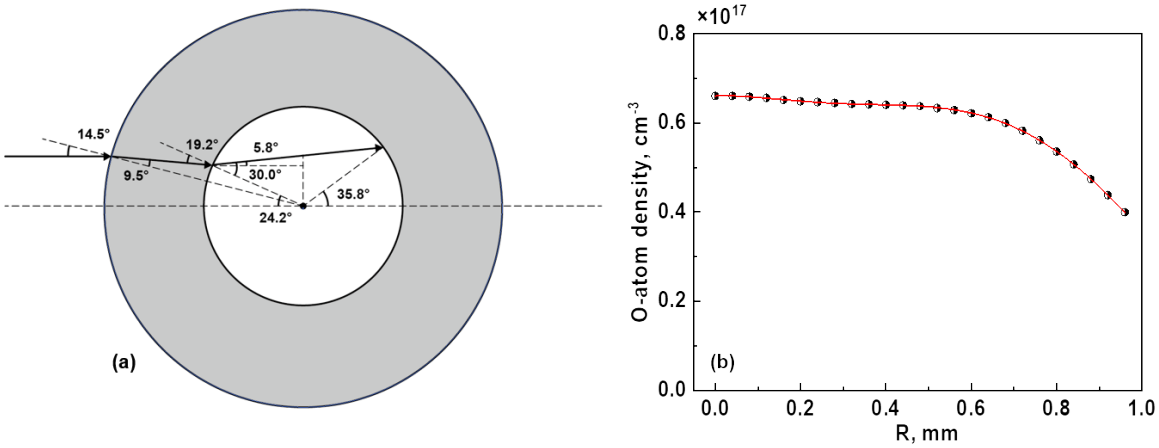

Figure A1. (a) Passing of the laser beam through the capillary: 2D ray tracing (upper half part). The diameter of the incident beam is 1 mm, the outer diameter of the capillary is 4 mm, and the inner diameter of the capillary is 2 mm. The refraction index for quartz at 225 nm is taken to be $n = 1.52$. (b) Radial distribution of O-atom density over the cross-section of the capillary in N_2 + 5% O_2, t = 15 μs. Symbols are the results of calculations, solid curve is a polynomial approximation.

In the second approach, 2D ray tracing was performed numerically. The incident laser beam was considered as a cylinder 1 mm in diameter. Figure A1(a) shows the results of ray tracing on the upper half part of the capillary cross-section. The divergence of the beam after passing through a thick curved capillary wall, playing the role of a short-focus diverging lens, is small: the beam deviation from the horizontal does not exceed 6°. Figure A1(b) presents a polynomial approximation of the numerically radial distribution of O-atoms in N_2 + 5% O_2 at 15 μs, which further gives us a 2D distribution across the cross-section of the capillary as shown in figure A2. As far as atomic

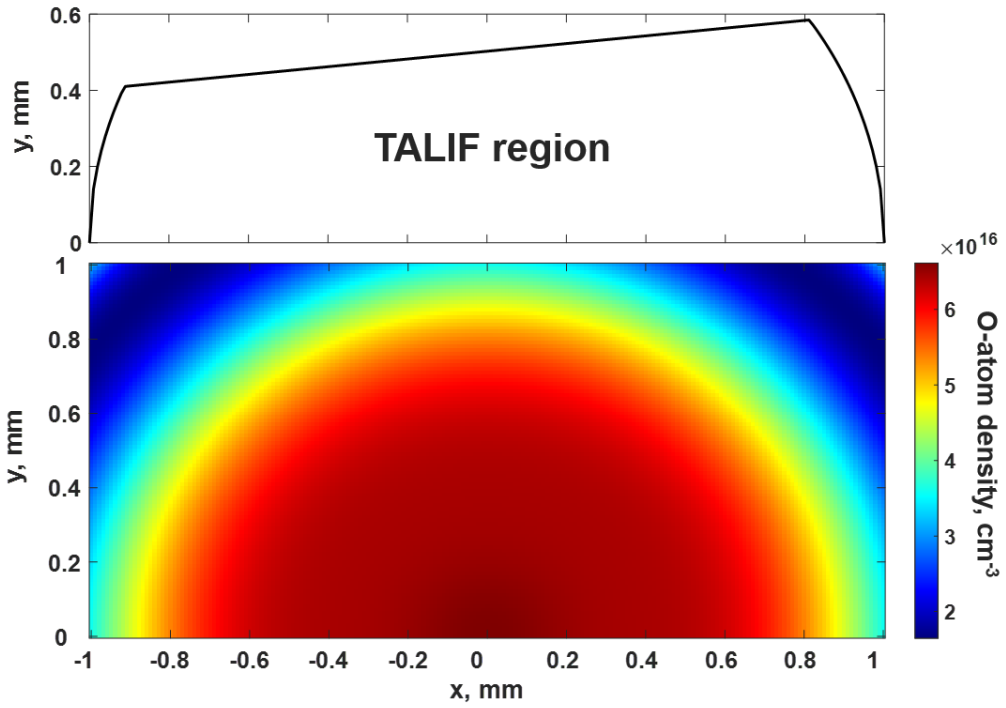

Figure A2. 2D-distribution of O-atoms density and the TALIF region covered by the laser beam over the half of cross-section of the capillary.

fluorescence is detected from the entire region of the laser beam inside the capillary, the traced pattern was convoluted with the calculated 2D distribution of O-atom density. The obtained result is that the systematic error caused by not taking into account the laser beam refraction and the 2D distribution of the O-atoms over the cross-section of the capillary is equal to 9%. The factor doesn't change with time after 5 μs due to the stabilization of the O-atom radial distribution.

The third approach was a rough experimental test supplementary to the analysis above. A methodologically ideal measurement of the fluorescence from a point near the axis of the tube from a very small area, no more than 0.2-0.3 mm in diameter, would result in a very high signal-to-noise ratio (SNR), making measurement impossible. Will note that a 1 cm wide slit in the metal screen 24 mm apart from the axis of the capillary served as a wide "natural" diaphragm when collecting the fluorescence light. To check how much the experimental result is influenced by the absence of a pinhole, the ratio of fluorescence of oxygen and xenon, S_O/S_{Xe}, was measured in a basic configuration under 27 mbar of N_2 + 5% O_2 at 5 μs and with a 1.5 mm diameter pinhole mounted on the slit in the screen at the distance 24 mm from the center of the capillary. The ratio S_O/S_{Xe} was found to be equal to 35.4 a.u. in the basic configuration and 37.5 with a 1.5 mm pinhole, providing 6% increase of the signal. Finally, will note that for the light passing from the capillary outside to the PMT, a thick capillary wall is a strongly diverging lens, so only the near-axis light of the collection system passes without being

Table A1. Accuracy of parameters of cross-section ratio determination in N_2+ 5% O_2 mixture.

Parameter	Relative uncertainty, %
$\frac{\delta\alpha}{\alpha}$	±3
$\frac{\delta n_O}{n_O}$	±1
$\frac{\delta n_{Xe}}{n_{Xe}}$	±1
$\frac{\delta\tau_0^{Xe}}{\tau_0^{Xe}}$	±5 [13]
$\frac{\delta\tau_0^{O}}{\tau_0^{O}}$	±4.9 [13]
$\frac{\delta(A_O+Q_O)}{A_O+Q_O}$	±5
$\frac{\delta(A_{Xe}+Q_{Xe})}{A_{Xe}+Q_{Xe}}$	±2
$\frac{\delta F_{Xe}}{F_{Xe}}$, $\frac{\delta F_O}{F_O}$	±2
$\frac{\delta\eta_{Xe}}{\eta_{Xe}}$, $\frac{\delta\eta_O}{\eta_O}$	±2
$\frac{\delta(S_{Xe}/I_{Xe}^2)}{S_{Xe}/I_{Xe}^2}$	±4
$\frac{\delta(S_O/I_O^2)}{S_O/I_O^2}$	±4

decreased in amplitude because of a strong divergence of light.

To summarize, it is necessary to set a factor α to correct the measurement due to O-atoms distribution with the laser beam profile in the capillary. Equation (A.2) was employed to calculate the total measurement error of $\sigma_{Xe}^{(2)}/\sigma_O^{(2)}$ in equation (27). Uncertainty $\delta\alpha/\alpha$ was estimated by the error of Abel transform (radial profile) of N_2 SPS emission, $\delta n_O/n_O$ and $\delta n_{Xe}/n_{Xe}$ were taken from the accuracy of the flow rate controller and the pressure sensor, $\delta\tau_0^{Xe}/\tau_0^{Xe}$ and $\delta\tau_0^{O}/\tau_0^{O}$ were measured in [13]. The errors related to the experimentally observed decay rate of the fluorescence, $\delta(A_{Xe}+Q_{Xe})/(A_{Xe}+Q_{Xe})$ and $\delta(A_O+Q_O)/(A_O+Q_O)$ were calculated based on the fitting processes of the experimental data illustrated in section 3.2.1. The uncertainty of the other parameters was taken directly from the measurements on the basis of stochastic errors. Table A1 lists the estimated relative uncertainty of each parameter in N_2+ 5% O_2 at 5 μs. The final values of error according to equation (A.2) are presented in table 4 together with obtained values of the ratio of the cross-sections.

$$\frac{\delta(\sigma_{Xe}^{(2)}/\sigma_O^{(2)})}{\sigma_{Xe}^{(2)}/\sigma_O^{(2)}} = \sqrt{\left(\frac{\delta\alpha}{\alpha}\right)^2+\left(\frac{\delta n_O}{n_O}\right)^2+\left(\frac{\delta n_{Xe}}{n_{Xe}}\right)^2+\left(\frac{\delta A_O}{A_O}\right)^2+\left(\frac{\delta A_{Xe}}{A_{Xe}}\right)^2+\left[\frac{\delta(A_{Xe}+Q_{Xe})}{A_{Xe}+Q_{Xe}}\right]^2+} \sqrt{\left[\frac{\delta(A_O+Q_O)}{A_O+Q_O}\right]^2+\left(\frac{\delta F_O}{F_O}\right)^2+\left(\frac{\delta F_{Xe}}{F_{Xe}}\right)^2+\left(\frac{\delta\eta_O}{\eta_O}\right)^2+\left(\frac{\delta\eta_{Xe}}{\eta_{Xe}}\right)^2+\left[\frac{\delta(S_{Xe}/I_{Xe}^2)}{S_{Xe}/I_{Xe}^2}\right]^2+\left[\frac{\delta(S_O/I_O^2)}{S_O/I_O^2}\right]^2}. \quad \text{(A.2)}$$

References

[1] Alves L L, Becker M M, van Dijk J, Gans T, Go D B, Stapelmann K, Tennyson J, Turner M M and Kushner M J 2023 Foundations of plasma standards *Plasma Sources Sci. Technol.* **32** 023001

[2] Stancu G D 2020 Two-photon absorption laser induced fluorescence: rate and density-matrix regimes for plasma diagnostics *Plasma Sources Sci. Technol.* **29** 054001

[3] Hay M, Parajuli P and Kulatilaka W D 2023 Simultaneous detection of three chemical species (NO, O, O_2) using a single broadband femtosecond laser *Proc. Combust. Inst.* **39** 1435–1444

[4] Bamford D J, Jusinski L E and Bischel W K 1986 Absolute two-photon absorption and three-photon ionization cross sections for atomic oxygen *Phys. Rev. A* **34** 185

[5] Saxon R P and Eichler J 1986 Theoretical calculation of two-photon absorption cross sections in atomic oxygen *Phys. Rev. A* **34** 199

[6] Bamford D J, Dyer M J and Bischel W K 1987 Single-frequency laser measurements of two-photon cross sections and Doppler-free spectra for atomic oxygen *Phys. Rev. A* **36** 3497

[7] Gottscho R A and Miller T A 1984 Optical techniques in plasma diagnostics *Pure Appl. Chem.* **56** 189–208

[8] Kohse-Hoinghaus K and Jefferies J B 2002 *Applied combustion diagnostics* (CRC Press)

[9] Kanaya Y, Sadanaga Y, Hirokawa J, Kajii Y and Akimoto H 2001 Development of a ground-based LIF instrument for measuring HO_x radicals: Instrumentation and calibrations *J. Atmos. Chem.* **38** 73–110

[10] Dreizler A, Lindenmaier S, Maas U, Hult J, Aldén M and Kaminski C 2000 Characterisation of a spark ignition system by planar laser-induced fluorescence of OH at high repetition rates and comparison with chemical kinetic calculations *Appl. Phys. B: Lasers Opt.* **70** 287–294

[11] Goehlich A, Kawetzki T and Döbele H 1998 On absolute calibration with xenon of laser diagnostic methods based on two-photon absorption *J. Chem. Phys.* **108** 9362–9370

[12] Niemi K, Schulz-Von Der Gathen V and Döbele H 2001 Absolute calibration of atomic density measurements by laser-induced fluorescence spectroscopy with two-photon excitation *J. Phys. D: Appl. Phys.* **34** 2330

[13] Niemi K, Schulz-Von Der Gathen V and Döbele H 2005 Absolute atomic oxygen density measurements by two-photon absorption laser-induced fluorescence spectroscopy in an RF-excited atmospheric pressure plasma jet *Plasma Sources Sci. Technol.* **14** 375

[14] Uddi M, Jiang N, Mintusov E, Adamovich I V and Lempert W R 2009 Atomic oxygen measurements in air and air/fuel nanosecond pulse discharges by two photon laser induced fluorescence *Proc. Combust. Inst.* **32** 929–936

[15] Reuter S, Winter J, Schmidt-Bleker A, Schroeder D, Lange H, Knake N, Schulz-Von Der Gathen V and Weltmann K 2012 Atomic oxygen in a cold argon plasma jet: TALIF spectroscopy in ambient air with modelling and measurements of ambient species diffusion *Plasma Sources Sci. Technol.* **21** 024005

[16] Pendleton S, Bowman S, Carter C, Gundersen M and Lempert W 2013 The production and evolution of atomic oxygen in the afterglow of streamer discharge in atmospheric pressure fuel/air mixtures *J. Phys. D: Appl. Phys.* **46** 305202

[17] Klochko A, Lemainque J, Booth J P and Starikovskaia S 2015 TALIF measurements of oxygen atom density in the afterglow of a capillary nanosecond discharge *Plasma Sources Sci. Technol.* **24** 025010

[18] Schmidt J B, Sands B, Scofield J, Gord J R and Roy S 2017 Comparison of femtosecond- and nanosecond-two-photon-absorption laser-induced fluorescence (TALIF) of atomic oxygen in atmospheric-pressure plasmas *Plasma Sources Sci. Technol.* **26** 055004

[19] Myers B, Barnat E and Stapelmann K 2021 Atomic oxygen density determination in the effluent of the COST reference source using in situ effective lifetime measurements in the presence of a liquid interface *J. Phys. D: Appl. Phys.* **54** 455202

[20] Brisset A, Bieniek M, Invernizzi L, Hasan M, Walsh J, Niemi K and Wagenaars E 2023 The

formation of O and H radicals in a pulsed discharge in atmospheric pressure helium with water vapour admixtures *Plasma Sources Sci. Technol.* **32** 065004

[21] Schmidt J B, Roy S, Kulatilaka W D, Shkurenkov I, Adamovich I V, Lempert W R and Gord J R 2016 Femtosecond, two-photon-absorption, laser-induced-fluorescence (fs-TALIF) imaging of atomic hydrogen and oxygen in non-equilibrium plasmas *J. Phys. D: Appl. Phys.* **50** 015204

[22] Annušová A, Marinov D, Booth J P, Sirse N, Da Silva M L, Lopez B and Guerra V 2018 Kinetics of highly vibrationally excited O_2(X) molecules in inductively-coupled oxygen plasmas *Plasma Sources Sci. Technol.* **27** 045006

[23] Schröter S, Bredin J, Gibson A R, West A, Dedrick J P, Wagenaars E, Niemi K, Gans T and O'Connell D 2020 The formation of atomic oxygen and hydrogen in atmospheric pressure plasmas containing humidity: picosecond two-photon absorption laser induced fluorescence and numerical simulations *Plasma Sources Sci. Technol.* **29** 105001

[24] Schröter S, Wijaikhum A, Gibson A R, West A, Davies H L, Minesi N, Dedrick J, Wagenaars E, De Oliveira N, Nahon L *et al.* 2018 Chemical kinetics in an atmospheric pressure helium plasma containing humidity *Phys. Chem. Chem. Phys.* **20** 24263–24286

[25] Blondel C, Alkhoury J, Jannaud T and Drag C 2020 The generalized two-photon excitation cross-section of Xe revisited *J. Phys. Conf. Ser.* **1412** 142012

[26] Drag C, Marmuse F and Blondel C 2021 Measurement of the two-photon excitation cross-section of the $6p'[3/2]_2$ and $6p'[1/2]_0$ levels of Xe I at the wavelengths 224.3 and 222.6 nm *Plasma Sources Sci. Technol.* **30** 075026

[27] Wubs J, Invernizzi L, Gazeli K, Macherius U, Lü X, Schrottke L, Lombardi G, Weltmann K D and van Helden J 2023 Validation of THz absorption spectroscopy by a comparison with ps-TALIF measurements of atomic oxygen densities *Appl. Phys. Lett.* **123**

[28] Klochko A V, Starikovskaia S M, Xiong Z and Kushner M J 2014 Investigation of capillary nanosecond discharges in air at moderate pressure: comparison of experiments and 2D numerical modelling *J. Phys. D: Appl. Phys.* **47** 365202

[29] Lepikhin N D, Klochko A V, Popov N A and Starikovskaia S M 2016 Long-lived plasma and fast quenching of $N_2(C^3\Pi_u)$ by electrons in the afterglow of a nanosecond capillary discharge in nitrogen *Plasma Sources Sci. Technol.* **25** 045003

[30] Lepikhin N D, Popov N A and Starikovskaia S M 2018 Fast gas heating and radial distribution of active species in nanosecond capillary discharge in pure nitrogen and N_2: O_2 mixtures *Plasma Sources Sci. Technol.* **27** 055005

[31] Vasilyak L M, Kostyuchenko S, Kudryavtsev N N and Filyugin I 1994 Fast ionisation waves under electrical breakdown conditions *Physics-Uspekhi* **37** 247

[32] Horiguchi H, Chang R and Setser D 1981 Radiative lifetimes and two-body collisional deactivation rate constants in Ar for Xe($5p\ ^5 6p$), Xe($5p\ ^5 6p$), and Xe($5p\ ^5 7p$) states *J. Chem. Phys.* **75** 1207–1218

[33] Pancheshnyi S, Starikovskaia S and Starikovskii A Y 1999 Population of nitrogen molecule electron states and structure of the fast ionization wave *J. Phys. D: Appl. Phys.* **32** 2219

[34] Wolfram—Alpha 2016 www.wolframalpha.com/faqs6.html Wolfram Alpha LLC

[35] Wolberg J 2006 *Data analysis using the method of least squares: extracting the most information from experiments* (Springer Science & Business Media)

[36] Park C 1989 *Nonequilibrium hypersonic aerothermodynamics* (New York, Chichester: J. Wiley and sons) ISBN 0-471-51093-9

[37] Radtsig A and Smirnov B 1980 *Handbook on atomic and molecular physics* (Atomizdat, Moscow)

[38] Popov N 2011 Kinetic processes initiated by a nanosecond high-current discharge in hot air *Plasma Phys. Rep.* **37** 807–815

[39] Laux C O, Spence T G, Kruger C H and Zare R N 2003 Optical diagnostics of atmospheric pressure air plasmas *Plasma Sources Sci. Technol.* **12** 125

[40] Popov N and Starikovskaia S 2022 Relaxation of electronic excitation in nitrogen/oxygen and fuel/air mixtures: fast gas heating in plasma-assisted ignition and flame stabilization *Prog.*

Energy Combust. Sci. **91** 100928

[41] Booth J P 1988 *Laser Studies of Species Involved in Plasma Etching Processes.* Ph.D. thesis University of Oxford

[42] Chng T L, Ding C, Naphade M, Goldberg B M, Adamovich I V and Starikovskaia S M 2020 Characterization of an optical pulse slicer for gas-phase electric field measurements using field-induced second harmonic generation *JINST* **15** C03005

[43] Chng T L, Naphade M, Goldberg B M, Adamovich I V and Starikovskaia S M 2020 Electric field vector measurements via nanosecond electric-field-induced second-harmonic generation *Opt. Lett.* **45** 1942–1945

[44] Hagelaar G and Pitchford L C 2005 Solving the Boltzmann equation to obtain electron transport coefficients and rate coefficients for fluid models *Plasma Sources Sci. Technol.* **14** 722

[45] Phelps A and Pitchford L 1985 Anisotropic scattering of electrons by N_2 and its effect on electron transport *Phys. Rev. A* **31** 2932

[46] Braginskiy O, Vasilieva A, Klopovskiy K, Kovalev A, Lopaev D, Proshina O, Rakhimova T and Rakhimov A 2005 Singlet oxygen generation in O_2 flow excited by RF discharge: I. Homogeneous discharge mode: α-mode *J. Phys. D: Appl. Phys.* **38** 3609

[47] Kovalev A, Lopaev D, Mankelevich Y A, Popov N, Rakhimova T, Poroykov A Y and Carroll D 2005 Kinetics of $O_2(b^1\Sigma_g^+)$ in oxygen RF discharges *J. Phys. D: Appl. Phys* **38** 2360–2370

[48] Tayal S and Zatsarinny O 2016 B-spline R-matrix-with-pseudostates approach for excitation and ionization of atomic oxygen by electron collisions *Phys. Rev. A* **94** 042707

[49] Bacri J and Medani A 1982 Electron diatomic molecule weighted total cross section calculation: III. main inelastic processes for N_2 and N_2^+ *Physica B+C* **112** 101–118

[50] Mintoussov E, Pendleton S, Gerbault F, Popov N and Starikovskaia S 2011 Fast gas heating in nitrogen–oxygen discharge plasma: II. Energy exchange in the afterglow of a volume nanosecond discharge at moderate pressures *J. Phys. D: Appl. Phys.* **44** 285202

[51] Popov N 2016 Pulsed nanosecond discharge in air at high specific deposited energy: fast gas heating and active particle production *Plasma Sources Sci. Technol.* **25** 044003

[52] Popov N 2013 Dissociation of nitrogen in a pulse-periodic dielectric barrier discharge at atmospheric pressure *Plasma Phys. Rep.* **39** 420–424

[53] Chng T L, Lepikhin N, Orel I, Popov N and Starikovskaia S M 2020 TALIF measurements of atomic nitrogen in the afterglow of a nanosecond capillary discharge *Plasma Sources Sci. Technol.* **29** 035017

[54] Florescu-Mitchell A and Mitchell J B A 2006 Dissociative recombination *Phys. Rep.* **430** 277–374

[55] Cosby P 1993 Electron-impact dissociation of nitrogen *J. Chem. Phys.* **98** 9544–9553

[56] Kossyi I, Kostinsky A Y, Matveyev A and Silakov V 1992 Kinetic scheme of the non-equilibrium discharge in nitrogen-oxygen mixtures *Plasma Sources Sci. Technol.* **1** 207

[57] Shkurenkov I, Burnette D, Lempert W R and Adamovich I V 2014 Kinetics of excited states and radicals in a nanosecond pulse discharge and afterglow in nitrogen and air *Plasma Sources Sci. Technol.* **23** 065003

[58] Galvão B, Varandas A, Braga J and Belchior J 2013 Electronic quenching of $N(^2D)$ by N_2: theoretical predictions, comparison with experimental rate constants, and impact on atmospheric modeling *J. Phys. Chem. Lett.* **4** 2292–2297

[59] Preda V C 1982 The Student distribution and the principle of maximum entropy *Annals of the Institute of Statistical Mathematics* **34** 335–338